RESEARCH ARTICLE

NANO · MICRO small

www.small-journal.com

Extensile Active Hydrogels Driven by Living FtsZ Polymers

Mikheil Kharbedia, Diego Herráez-Aguilar, Macarena Calero, Horacio López-Menendez, Clara Luque-Rioja, Lara H. Moleiro, Cruz Santos, Pilar Lillo, and Francisco Monroy**

Embedding living polymers that consume chemical energy into synthetic gels offers a route to soft materials that self-regulate their mechanical state. Here, The bacterial cytokinetic protein FtsZ is integrated within a polyacrylamide network to create an active extensile hydrogel. Upon post-gelation activation with Mg^{2+} and GTP, FtsZ filaments treadmill and exert internal stresses that drive isotropic swelling and mechanical softening. These responses is described using a Flory–Rehner swelling framework, where activity-induced volume expansion lowers the polymer volume fraction and, consequently, the elastic modulus. Normalizing the measured moduli to the FR baseline isolates an additional, rate-dependent softening that arises from living FtsZ polymer dynamics. Rheological analysis reveals that biochemical energy input modulates the elastic state of a pre-formed network through active swelling and strain-dependent fluidization, establishing a minimal model for living-polymer-driven soft materials.

1. Introduction

Nature builds active force generators from biopolymers,[1–4] which consume nucleotide energy to drive motion across molecular scales.[5–8] Such energy-dissipating polymers enable living systems to generate forces autonomously, regulating mechanical processes essential for life.[9,10] Inspired by these biological principles, researchers have long sought to design hybrid hydrogels that reproduce adaptive, force-responsive behaviors for biomedical[11] and technological applications,[12] including soft robotics' developments.[13,14] Functionality-driven hydrogels adapt their viscoelastic properties in response to mechanical stress and environmental signals such as temperature, osmotic pressure, and pH,[15–20] a versatility that opens avenues from biosensing to drug delivery. Their highly hydrated, compliant networks are ideal for embedding bioactive components, enabling hybrid materials with emergent properties distinct from the passive matrix.[15–20] Among such mechanoresponsive biomolecules, including shape-altering proteins,[21,22] molecular motors,[23–25] and living cytoskeletal filaments,[26,27] can act as mechanical primers converting chemical energy into localized, non-thermal forces.[20] When incorporated at low concentrations to avoid self-percolation or crowding, these actuators can generate spatially distributed active stresses, provided the host matrix is sufficiently soft to accommodate them.

Active hydrogels incorporating living biofilaments are categorized as either contractile, where embedded force-generating actuators (e.g., actomyosin[24] or microtubule-kinesin[25] systems) exert pulling forces to compact the material, or extensile, where internal filaments generate pushing forces that expand and soften the matrix. While contractile gels have been widely demonstrated,[1–8] biologically based extensile gels remain

M. Kharbedia, D. Herráez-Aguilar, M. Calero, H. López-Menendez, C. Luque-Rioja, L. H. Moleiro, F. Monroy
Department of Physical Chemistry
Universidad Complutense
Ciudad Universitaria
Madrid 28040, Spain
E-mail: diego.herraez@ufv.es; monroy@ucm.es

M. Kharbedia, M. Calero, H. López-Menendez, C. Luque-Rioja, L. H. Moleiro, F. Monroy
Unit of Translational Biophysics
Instituto de Investigación Hospital Doce de Octubre (i+12)
Av. Córdoba, Madrid 28041, Spain

The ORCID identification number(s) for the author(s) of this article can be found under https://doi.org/10.1002/smll.202510218

DOI: 10.1002/smll.202510218

D. Herráez-Aguilar, C. Santos
Instituto de Investigaciones Biosanitarias
Universidad Francisco de Vitoria
Ctra. M-515 Pozuelo-Majadahonda Km 1,800, Pozuelo de Alarcón, Madrid 28223, Spain

M. Calero
Faculty of Health Sciences - HM Hospitals
Camilo Jose Cela University
Villanueva de la Cañada, Madrid 28692, España

M. Calero
HM Hospitals Health Research Institute
Madrid 28015, Spain

P. Lillo
Instituto de Química Física "Blas Cabrera"
C/ Serrano 119, Madrid 28006, Spain

underexplored, especially when internal stresses arise from isotropic, stochastic filament dynamics. A gap therefore persists in developing extensile hydrogels built from living polymers and in the frameworks needed to describe their non-equilibrium mechanics.

In this work, we harness FtsZ, a bacterial division protein that forms GTP-dependent, filaments.[28–30] GTP binding enables filament assembly,[28] whereas Mg^{2+}-dependent hydrolysis sustains subunit turnover,[31] establishing FtsZ filaments as living polymers.[32,33] We fabricate hybrid hydrogels that exhibit extensile responses driven by these polymerization-mediated forces. Embedding randomly oriented, GTP-fueled FtsZ filaments within a polyacrylamide (PA) matrix creates a composite in which treadmilling generates internal stresses that soften and fluidize the host, yielding self-actuated extensibility. In contrast to classical contractile systems (actomyosin,[23,24] tubulin filaments[8] and microtubule-kinesin),[25] FtsZ-driven PA hydrogels display active softening akin to hyperfluidity, acting as activatable metamaterials with negative mechanical susceptibility, amplifying applied stress rather than resisting it.

From a theoretical standpoint, the mechanics of swollen polymer networks are classically described by the Flory–Rehner (FR) model,[34,35] which relates equilibrium swelling and modulus to polymer volume fraction,[36] crosslink density,[37] and solvent quality.[35] This framework provides a microscopic link between swelling and elastic response;[35] a natural baseline for identifying activity-induced deviations. We extend this view by embedding FtsZ activity into the FR description, establishing a microscopic up to continuum bridge that unifies swelling-controlled elasticity with active stress generation. In this context, we introduce the concept of metamaterial permittivity, defined as an activity-dependent amplification factor that relates the baseline modulus of the passive matrix to the reduced effective modulus of the active composite. Such unconventional behavior is analogous to the dielectric response of acoustic and plasmonic metamaterials,[38] where resonance produces field amplification under negative susceptibility to external field. Building on this principle, we adapt Landau-type bifurcation with a Soft Glassy Rheology (SGR) dynamic framework,[39] using FR–model[35] to set the reference that separates passive dilution from genuine active softening. This multiscale SGRL-FR framework allows us to define an activity-dependent effective permittivity that captures the amplification of applied stresses in extensile gels.

In prior work,[40] we developed a framework for active forces in FtsZ-based hydrogels, highlighting how treadmilling-driven hydrodynamics promote active reptation in swollen matrices. Here we extend it to capture weakening with increasing strain rate and frequency, while anchoring mechanical responses to the FR–baseline via swelling-dependent moduli. This reveals a mechanism of self-actuated extensibility distinct from equilibrium matrix resistance, enabling programmable soft materials based on living polymers. The resulting FtsZ-based composites invert the usual resistive response to actuate as mechanical metamaterials, suggesting applications in tissue engineering, drug delivery, regenerative scaffolds, soft robotics, and other biointegrated technologies. This positions FtsZ-based gels as a versatile model for active soft materials driven by living polymers, as emphasized in recent active-matter roadmaps.[41]

2. FtsZ Gel Hybridization Rationale

FtsZ is a conserved bacterial cytoskeletal protein that polymerizes into GTP-dependent filaments during cytokinesis.[42–44] Above the critical concentration, GTP binding enables assembly and Mg^{2+}-dependent hydrolysis drives subunit turnover, yielding living, treadmilling polymers.[45,46] Functionally, treadmilling FtsZ serves both as a force generator for membrane constriction,[47,48] and as a dynamic scaffold for septal growth.[49] Polymerization is reversible, Mg^{2+}-dependent, dependent, and occurs above ≈0.1 mg mL^{-1} in vitro.[50] Each FtsZ monomer hydrolyzes one GTP per turnover cycle, so the polymer continuously remodels its structure.[49–53] Reconstituted FtsZ filaments operate autonomously in biomimetic systems,[54–57] demonstrating their capacity for self-actuated mechanical activity. Although the precise mechanism of cytokinetic force generation remains debated,[58–60] these results identify FtsZ filaments as promising actuators for synthetic soft-matter devices. Building on this foundation, we engineered extensile hydrogels by embedding GTP-fueled, randomly oriented FtsZ filaments within compliant PA networks. **Figure 1A** illustrates FtsZ physically entrapped after PA gelation and, upon Mg^{2+}/GTP activation, forming interpenetrating (non-fused) filaments that generate distributed extensile stresses within the matrix.

As summarized in Figure 1B, Mg^{2+}/GTP activation yields living, treadmilling polymers that generate spatially distributed extensile stresses, which soften the host matrix and produce active swelling and spontaneous extensibility. Multiscale modeling indicates that these emergent properties arise from activity-induced modulation of network elasticity under partial release of reptation constraints,[40] confirming that cooperative filament activity underlies the observed mechanical softening in FtsZ–PA hydrogels.[40]

3. Results

As above depicted in Figure 1, we studied hybrid polyacrylamide (PA) hydrogels in which recombinant FtsZ is physically entrapped within the crosslinked PA network. GTP binding renders FtsZ assembly-competent, driving filament formation above the critical concentration.[28] In the presence of Mg^{2+}, GTP hydrolysis sustains rapid subunit turnover, producing filament treadmilling (living-polymer behavior).[31–33] Passive filament conditions (no Mg^{2+}) keep FtsZ unmobile, hence defining the Flory–Rehner (FR) baseline.[34] Active conditions are generated by adding Mg^{2+} to pre-formed gels, which triggers GTPase-coupled treadmilling, thereby generating internal extensile stresses.

3.1. Structural Remodeling by Embedded FtsZ Filaments

To assess the microstructural impact of embedding FtsZ filaments into crosslinked PA hydrogels, we performed scanning electron microscopy (SEM) on samples with two crosslinking densities: 2.5% and 7%, corresponding to low- and high-rigidity states. **Figure 2** shows SEM images of the hydrogel microstructure. For each PA formulation, control gels without FtsZ are compared with counterpart gels prepared with FtsZ in the presence of GTP (Figure 2A,B, left and right panels, respectively).

NANO · MICRO small
www.small-journal.com

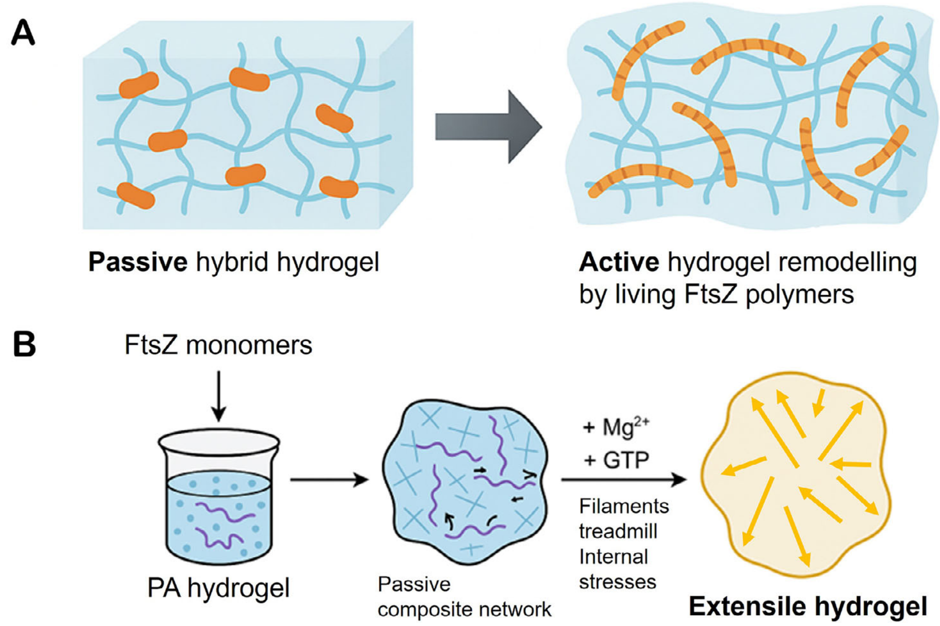

Figure 1. A) Conceptual representation of FtsZ–polyacrylamide (PA) hybrid gels. In the passive state, FtsZ monomers are entrapped within the PA mesh but remain inactive. Upon GTP/Mg^{2+} activation, FtsZ self-assembles into treadmilling filaments that generate distributed extensile stresses, driving hydrogel remodeling (active softening, swelling, and extensibility). FtsZ is not covalently linked to PA: filaments interpenetrate the crosslinked network without fusion, yielding a mechanically coupled but non-bonded composite. B) Experimental workflow. Recombinant FtsZ is mixed with acrylamide precursors to form a passive composite; post-gelation addition of Mg^{2+} (with hydrolyzable GTP previously added) triggers filament treadmilling and internal stress generation, transforming the gel into an extensile active material with self-driven emergent behavior.

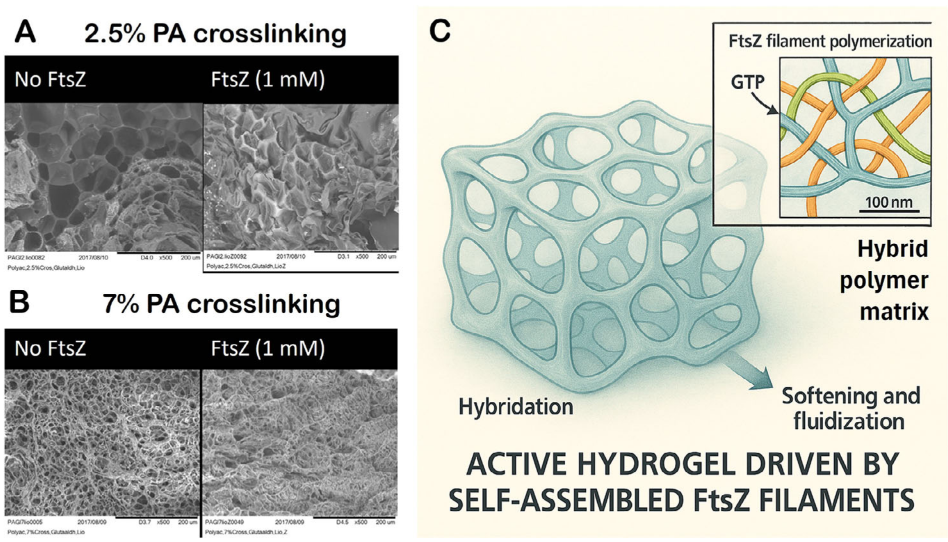

Figure 2. SEM of FtsZ–polyacrylamide (PA) hybrid hydrogels (10% polymer fraction): A) 2.5% PA crosslinking and B) 7% PA crosslinking, each shown without FtsZ (left) and with 1 mM FtsZ (right; prepared with GTP but without Mg^{2+}, i.e., passive polymerization, non-treadmilling). At 2.5% PA the passive gel displays a polygonal open mesh; with FtsZ the dehydrated texture becomes more corrugated/fibrillar. At 7% PA the matrix is denser and differences with FtsZ are subtler. These contrasts reflect a hybrid PA–FtsZ composite under static dried conditions, not direct measurement of hydrated pore size. C) Schematic. The main panel sketches the poroelastic PA foam (image generated by GPT 4o DALL-E); the inset shows an interpenetrating microscopic network of PA strands (blue) with FtsZ filaments (orange = GTP/Mg^{2+}-activated, treadmilling; green = passive filaments) that can soften or stiffen the matrix (inset scale bar: 100 nm). This poroelastic depiction aligns with the Flory–Rehner swelling baseline used to interpret the experiments.

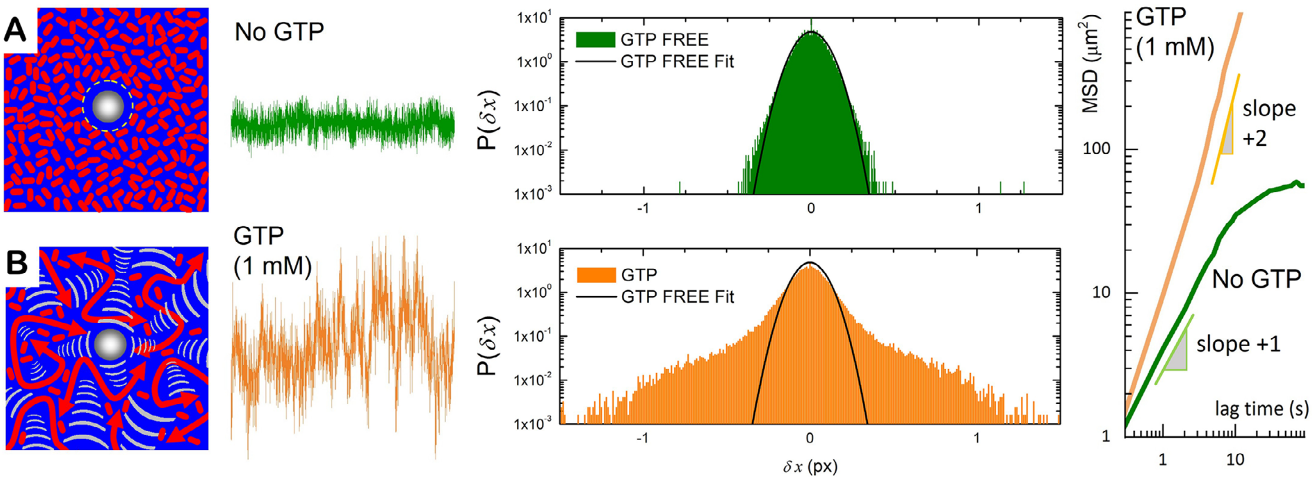

Figure 3. Mechanical activity of FtsZ filaments probed by tracer microrheology. Microparticles (diameter 1 μm) embedded in the gel report local fluctuations. A) Passive monomer solution (no GTP): FtsZ remains unpolymrized and no internal activity is present (schematic, left). The position trace shows small, confined fluctuations; the displacement PDF (green) is well fit by a Gaussian, consistent with a harmonic trap in a viscoelastic medium. B) Active (+1 mM GTP): FtsZ polymerizes and treadmills (schematic, left), producing large, intermittent kicks. The time series shows enhanced excursions, and the displacement PDF (orange) is heavy-tailed (non-Gaussian), evidencing out-of-equilibrium forcing. *Rightmost panels:* Mean-square displacement (MSD) analysis reveals a transition from near-diffusive scaling in the passive state ($MSD \sim t$, with an initial confinement time of ≈10 s) to superdiffusive/ballistic motion under activation ($MSD \sim t^2$). These signatures identify FtsZ filaments as internal actuators that inject mechanical energy into the matrix. Imaging used a 40 × objective; 1 pixel corresponds to 120 nm.

This protocol uses GTP without Mg^{2+}, assembling static FtsZ oligomers physically entrapped prior to fixation and imaging (see Methods). At 2.5% crosslinking (Figure 2A), the PA gels exhibited large, well-defined porous domains with a polygonal architecture (Figure 2A, left), indicative of low-density, open-mesh structures. Upon incorporation of polymerizing FtsZ (Figure 2A, right), the matrix showed substantial architectural disruption: the regular geometry was replaced by a more irregular, fibrillar texture with signs of internal wrinkling and anisotropic annealing of the polymer mesh. Under these static conditions, we interpret these features as signatures of hybridization and confinement within an interpenetrating, non-fused PA–FtsZ composite, rather than evidence of activity-driven remodeling or covalent bond scission. At 7% crosslinking (Figure 2B), the matrix displayed a much denser and more isotropic morphology, with small, interlinked mesopores and a relatively uniform texture in the absence of FtsZ (Figure 2B, left). When FtsZ was included at this higher crosslinking density (Figure 2B, right), only subtle changes were observed, consistent with the greater resistance of stiffer networks to confinement-induced texturing during dehydration. Importantly, SEM images were acquired on dehydrated specimens; the corrugated domains reflect preparation in vacuum and should not be taken as native hydrated mesh dimensions. Taken together, the SEM data support the formation of an interpenetrating, non-fused PA–FtsZ composite whose morphological imprint is most evident at lower crosslinking. Because specimens are dehydrated for SEM, the micron-scale features should be interpreted as mesostructural corrugation/collapse of the dried scaffold, not as the native nm-scale mesh of hydrated PA. We therefore use SEM qualitatively to compare textures between conditions (see also cartoon in Figure 2C, which schematizes the interpenetrating microstructure).

3.2. Living FtsZ Polymers Induce Non-Equilibrium Fluctuations

Figure 3 probes the mechanical activity of FtsZ using high-speed videomicroscopy of embedded probe particles. In the absence of GTP, the medium contains only monomeric FtsZ, and particle probing displacements are Gaussian (Figure 3A), consistent with thermal confinement in a harmonic trap, compatible with an Ornstein–Uhlenbeck process, $MSD_{pass}(t) \approx 4Dt_{conf}(1 - e^{-t/t_{conf}}) \approx 4Dt$, with confinement time $t_{conf} \approx 10\,s$ (Figure 3, rightmost panel). Upon GTP addition with Mg^{2+}, filaments polymerize and treadmilling renders the system active: the displacement PDFs develop heavy, symmetric tails (Figure 3B), and the MSD exhibits a superdiffusive window with ballistic-like scaling: $MSD_{act}(t) \approx c_F^2 t^2$, with a fitted propulsion velocity $c_F = (2.7 \pm 0.3)\,\mu m/s$ (Figure 3, rightmost panel). Thus, activation converts passive confinement into a nonequilibrium fluctuating state driven by GTP consumption. We model displacement statistics as, $P(x) = exp(-\ U_{conf}/k_B T)$, corresponding to a Boltzmann distribution. In the passive state, $U_{conf}^{(pass)} = k_{pass}x^2/2$, with $k_{pass} = (15.3 \pm 1.8) pN/\mu m$. After activation, the best fit requires a cusp term: $U_{conf}^{(act)} \approx k_{act}x^2/2 - F_0|x| + \mathcal{O}(x^4)$, capturing long-displacement treadmilling FtsZ activity, with $k_{act} = (10 \pm 3) pN/\mu m$ ($< k_{pass}$ trend to softening; two-sided Student *t*-test $P \approx 0.11$, $n = 3$), and a characteristic force $F_0 = (50 \pm 4)\,pN$, notably higher than the force typically exerted by actomyosin strokes.[23,24] An illustrative upper-bound energy per burst, $E_K = F_0\Lambda_0$, with characteristic displacements, $\Lambda_0 \approx 100\,nm$, corresponds to $E_K \approx 5 \times 10^{-18}\,J \approx 10^3\,k_B T$, sufficient to eject the particle from its thermal trap and produce the observed bursts. The non-Gaussian broadening of $P(x)$, together with superdiffusive MSD provides the most robust evidence of activation (Figure 3);

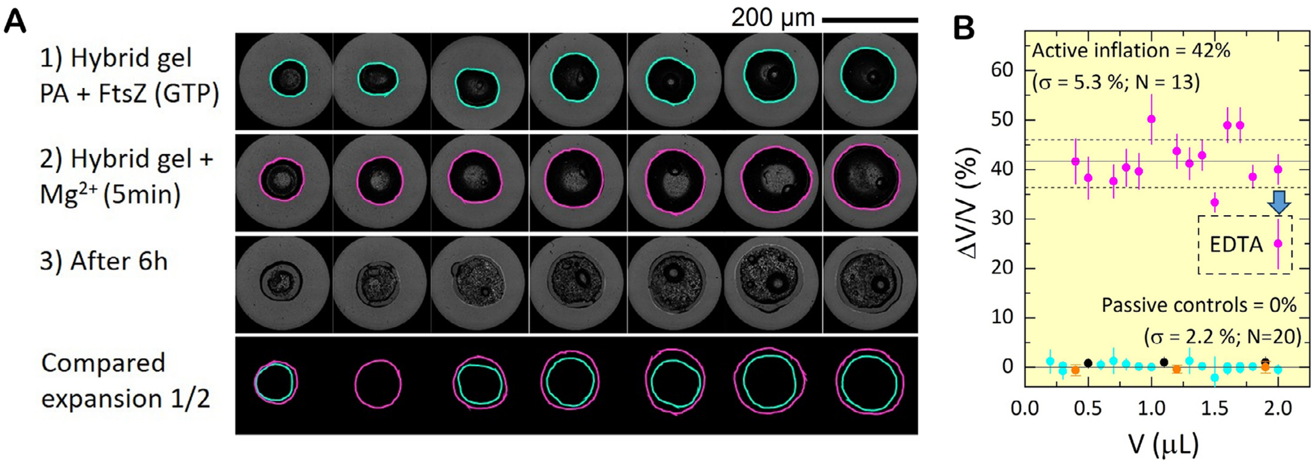

Figure 4. Hydrostatic swelling of hybrid FtsZ–polyacrylamide (PA) microgels upon GTP-dependent activation (with ionic controls and EDTA deactivation test). A) *Left strips' panel:* ime-lapse bright-field images of single microgels: 1) Hybrid PA+FtsZ microgels prepared with GTP but without Mg^{2+} show no size change (cyan contours); 2) Adding Mg^{2+} (2 mм) to the same microgels triggers FtsZ polymerization/treadmilling and rapid inflation (magenta contours, 5 min); 3) Images at 6 h illustrate the maintained swollen state. *Bottom row*: Superimposed pre-/post-activation contours of each droplet emphasize the extent of expansion. Scale bar, 200 µm. B) Morphometric analysis of fractional volume change ΔV/V vs initial droplet volume. Active (Mg^{2+} + GTP) microgels (magenta) exhibit an average inflation of ≈42% (σ = 5.3%, N = 13). Passive controls remain stable near 0%: GTP/no-Mg^{2+} (cyan), PA-only with Mg^{2+} 2 mм (black), and iso-osmotic KCl 2 mм (orange) (overall σ = 2.2%, N = 20). EDTA chelation applied after activation (boxed point, arrow) partially reduces the swollen volume, indicating attenuation (not full reversal) of activity in bulk gels due to non-uniform Mg^{2+} removal.

a two-sample Kolmogorov–Smirnov test on independent subsamples rejects equality of passive vs. active distributions ($P < 0.01$, two-sided), with separation across both central quantiles and tails. Overall, these data show that treadmilling FtsZ filaments act as internal mechanical actuators, simultaneously injecting localized stress and reducing effective confinement, consistent with an extensible active-gel state.

3.3. Structural Extensibility by Internal Activation: Swelling Assays

To probe hydrostatic extensibility under internal activation, we produced PA–FtsZ microgel droplets (≈100 µm diameter) with a millifluidic needle injector (see Experimental Section). The precursor (3% acrylamide, 0.07% bis-acrylamide, 0.5 mg mL^{-1} FtsZ, 1 mм GTP, no Mg^{2+}) was polymerized and equilibrated overnight in isotonic buffer. Swelling was then monitored on these pre-formed PA+FtsZ+GTP droplets while activating the same specimens by adding Mg^{2+}. As shown in **Figure** 4A, pre-formed PA+FtsZ+GTP microgels maintained in Mg^{2+}-free buffer retained their original size and shape (cyan contours), whereas addition of $MgCl_2$ (2 mм) to the same droplets triggered a rapid radial expansion (magenta contours), reaching ΔV/V = 42% ± 5% within ≈5 min and remaining elevated for hours. PA-only + Mg^{2+} (2 mм) and iso-osmotic KCl (3 mм) controls showed no measurable swelling (≈0%), excluding osmotic/ionic artifacts. Quantitative morphometrics (Figure 4B) confirms this robust, reproducible inflation, establishing that GTP-activated FtsZ polymerization generates internal extensile stresses capable of deforming the PA network. Over longer times (≈6 h), activated droplets gradually deflated as GTP was exhausted; chelation of Mg^{2+} with EDTA produced partial deswelling, indicating incomplete, spatially heterogeneous deactivation in bulk. Together, these observations demonstrate activity-controlled structural extensibility with transient softening in FtsZ–PA microgels. We defer full cycling to future work using microfluidic exchange or photo-caged cofactors to achieve rapid, homogeneous deactivation.

3.4. Active FtsZ Polymerization Mechanical Softening and Fluidization

We quantified the rheological response by tracking the shear modulus (G′) and viscosity (η) of pre-equilibrated PA–FtsZ+GTP gels, then triggered treadmilling post-gelation by adding 2 mм $MgCl_2$ at 37 °C to the same specimen, hereafter "active"; "passive" denotes Mg^{2+}-free (GTP present) or formulations lacking GTP or FtsZ. As shown in **Figure 5**, passive gels display only baseline evolution, whereas Mg^{2+} addition produces a sudden, large drop in both G′ and η, marking a transition to an actively softened, hyperfluidized state (Figure 5B, yellow panels). This jump reflects the onset of internally generated extensile stresses from treadmilling FtsZ filaments that remodel the network; the activated state remains stable for > 8 h until GTP exhaustion. In contrast, negative controls—no GTP or no FtsZ, show no softening and only minor drift attributable to passive swelling (Figure 5C, gray panels). The GTP/Mg^{2+}-specific onset and long-lived response confirm that the mechanical transition is activity-driven, not osmotic in origin, demonstrating a biohybrid gel whose viscoelasticity is modulated from within by living FtsZ polymers. To mechanistically rationalize the activation-induced drop in rigidity and viscosity observed in Figure 5, we next develop a quantitative framework that separates passive swelling from genuine activity-driven softening and captures the observed rate and strain dependences.

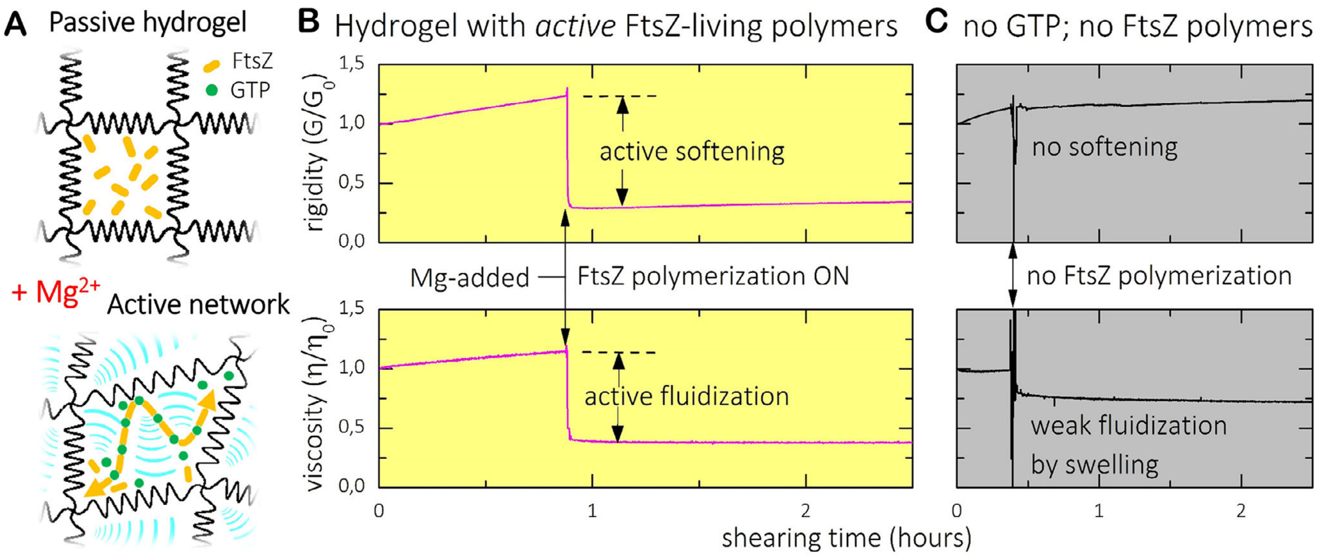

Figure 5. Active softening and fluidization of FtsZ-embedded hydrogels. Left, schematic: a passive polyacrylamide (PA) hydrogel with dispersed FtsZ monomers (top) becomes an active extensile network upon post-gelation addition of Mg^{2+} in the presence of GTP (bottom). Center (yellow background): real-time rheology of the same PA–FtsZ+GTP specimen shows an abrupt drop in rigidity G' (plotted as G/G_0) and viscosity η (plotted as η/η_0) immediately after Mg^{2+} addition, indicating activation-induced softening and fluidization; the activated state remains stable for mor than 8 h until GTP exhaustion. Right (gray background): controls without GTP (no FtsZ filaments) show no softening and only minor fluidization attributable to passive swelling in the presence of FtsZ monomers. Together, these data demonstrate that internal FtsZ treadmilling reduces matrix resistance via extensile stresses, yielding an actively swellable, reconfigurable hydrogel.

3.5. Active Softening Theory Flory–Rehner–Landau (FRL) Modeling under Soft Glassy rheology Dressing

We adopt a Flory–Rehner (FR)–first passive description, in which equilibrium swelling sets a baseline rigidity $G_0(\phi)$ at polymer fraction ϕ (Note N1, Supporting Information). Activity is then encoded via a Landau-type susceptibility that can assume negative values for extensile responses (Note N2, Supporting Information), and Soft-Glassy-Rheology (SGR) dressing to capture the observed frequency- (ω) and strain- (γ) dependences (Note N3, Supporting Information). This FR–Landau–SGR construction defines the mechanical permittivity (ϵ) used to normalize all measurements and will henceforth serve as the theoretical framework for analyzing composition-dependent rheological maps and frequency-dependent spectra. Specifically, the passive modulus scales with polymer fraction,

$$G_0\left(\phi, c_0\right) = c_0 k_B T\, \phi^{\alpha}, \tag{1}$$

with c_0 the effective strand density at gelation,[34,35] and α determined experimentally. Classical affine rubber-elasticity predicts $\alpha \approx 1$ (often quoted in the range 1–1.5, depending on solvent quality and finite-chain extensibility),[61] whereas non-affine/percolation theories for tenuous networks predict $\alpha \approx 3$ (near the gel point as approaching $\phi \to \phi^*$)[20]. Reported moduli $G(\phi)$ are referenced to this FR–first baseline via the mechanical permittivity

$$\epsilon\left(\phi, \gamma\right) \equiv \frac{G}{G_0} = 1 + \chi \tag{2}$$

where χ is a dimensionless susceptibility describing how the swollen meshwork responds to internally generated stresses under an applied strain (γ). Thus, $\epsilon \approx 1$ indicates dilution-only changes, $\epsilon < 1$ denotes activity-induced softening (extensile), $\epsilon > 1$ denotes hardening (contractile). Mechanical stability requires $\epsilon > 0$ (i.e., $\chi > -1$).

3.5.1. Activity Encoding (Landau Layer)

Activity enters through a scalar order parameter $\Gamma(c/c_0)$. Near onset we write $\epsilon \approx 1 + \chi(\Gamma)$, with $\chi < 0$ for extensile softening ($\Gamma > 0$). The stationarity condition, near-onset branches, and stability criteria are in Note N2 Supporting Information), where activity–swelling feedback (activity lowers ϕ, further reducing G) is treated explicitly.

3.5.2. Frequency/Strain Dependence (SGR Dressing)

Departures from the FR baseline with rate or amplitude are captured by a soft-glassy rheology kernel scaled by ϵ, as follows:

$$\tilde{G}\left(\omega, \gamma\right) = \epsilon\left(\gamma\right) \tilde{G}_{SGR}\left[\omega; x\left(\gamma\right), \tau\right] + i\omega\eta_{\infty}, \tag{3}$$

where $x(\gamma)$ is an effective noise temperature (increasing with activity/dilution), τ a structural time, and η_∞ the high-frequency viscosity.[39] This compact form reproduces the observed power-law spectra and strain-weakening; derivations, asymptotics, and the fitting protocol are in Note N3 (Supporting Information).

3.5.3. Activity–Swelling Feedback

The coupled FR–Landau construction yields a fit-ready $\chi(\phi, \gamma)$ that makes explicit how extensile activity lowers the effective onset via dilution; the expression and coefficients are given in the

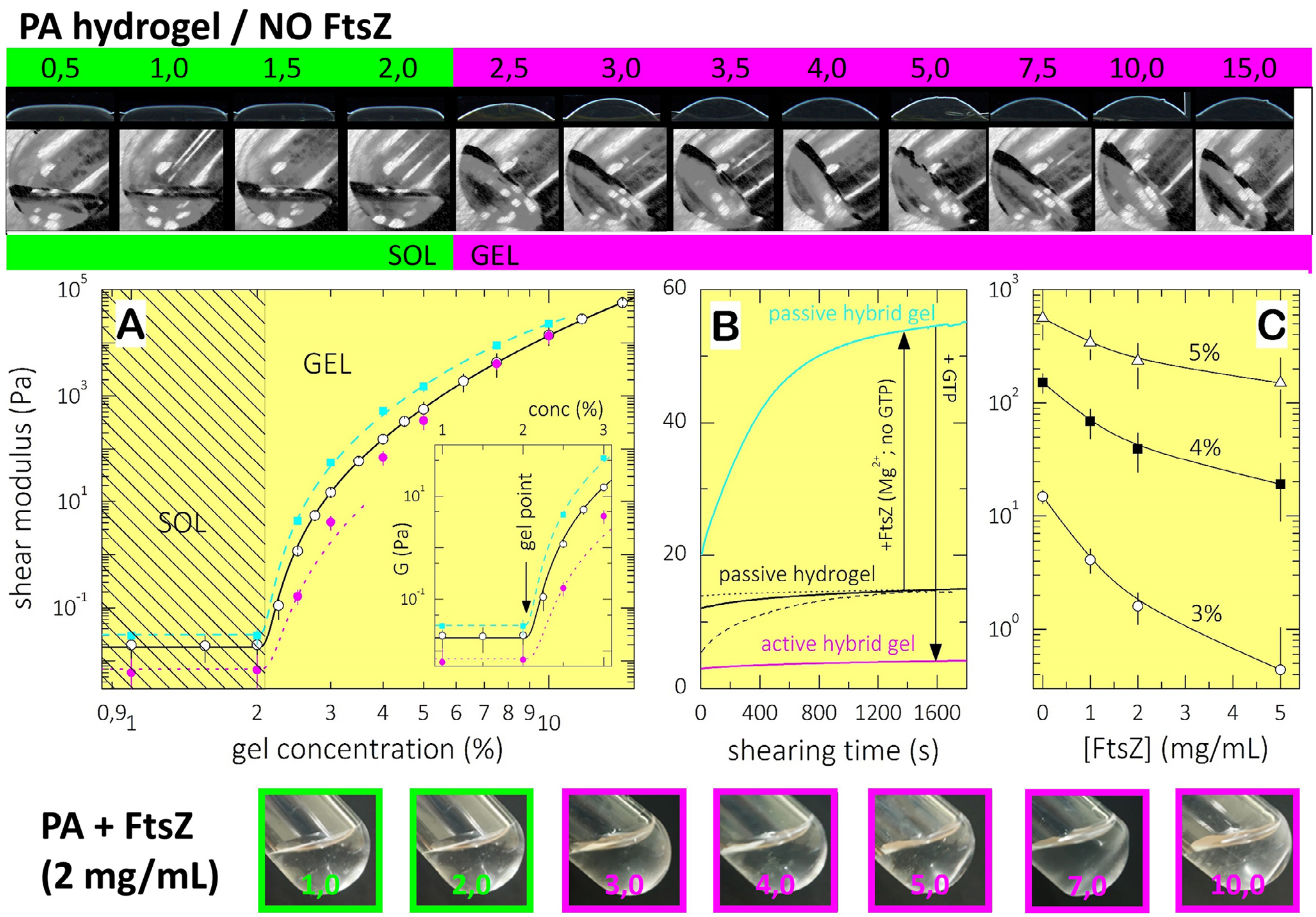

Figure 6. Composition-dependent rheology of passive and active FtsZ–PA hydrogels. Top strip: Tilt tests across PA concentrations (0.5%–15%). Pure PA (no FtsZ) transitions from liquid-like sol (green, $\phi < 2.5\%$) to solid-like gel (magenta, $\phi > 2.5\%$), retaining shape upon tilting. A) Sol–gel transition: storage modulus G′G′G′ vs PA concentration for passive PA (black), passive hybrids with FtsZ but no GTP (cyan), and active hybrids with GTP/Mg^{2+}-polymerized FtsZ (magenta). Solid lines are best fits to Equation (1) (FR/percolation scaling) and the inset (log–log) highlights the percolation-like onset near $\phi^* \approx 2.5$. Active hybrids lie systematically below the passive curves, evidencing extensile softening by living FtsZ filaments. B) Time evolution: under oscillatory shear, passive matrices (including FtsZ–no-GTP blends) show gradual stiffening; upon GTP-triggered activation (arrow), active hybrids display an abrupt drop in G′, consistent with internally driven fluidization. C) Dose response: terminal G′ vs FtsZ concentration for 3%, 4%, and 5% PA shows monotonic softening with [FtsZ], strongest near the percolation threshold (3% PA). Bottom strip: Tilt tests of FtsZ hybrids at fixed [FtsZ] = 2 mg mL^{-1} and varying PA (1%–10%; values in frames) show persistent collapse/liquid-like behavior across the gel regime, in contrast to pure PA gels above the sol–gel threshold. Figure S1 (Supporting Information) reports G′(ϕ), G″(ϕ), and tan $\delta(\phi)$=G″/G′ under tilt settings for active, non-activated (no Mg^{2+}), and PA-only samples; all confirm tan $\delta < 1$, verifying the reduced viscosity / enhanced creep compliance unique to the active gel.

(Notes N2 and N3, Supporting Information). In practice, we first fit passive $G_0(\phi)$ to obtain c_0 and α (FR–baseline); then report $\epsilon(\gamma) = G/G_0$ to separate swelling from true activity; finally we apply the Landau–SGR layers, where ϵ departs from unity to quantify activity-driven softening and its frequency/strain dependence (see Note N1, Supporting Information). With the FR baseline and the activity-dependent susceptibility in place, we now test the model against composition-dependent rigidity and dose responses, using Equation (1) for the FR fits and the permittivity normalization to isolate activity.

3.6. Network Composition Effects: Elasticity Mapping

In **Figure 6**, we map mechanics across composition and activity by combining time-resolved rheology with tube tilting assays. The top photo strip visualizes the sol–gel transition of passive PA in inclined test tubes: shape stability emerges sharply above ≈2.5% acrylamide. Rheologically, Figure 6A shows the terminal shear modulus G′ vs PA polymer density for three formulations: PA-only (black), PA + FtsZ (GTP, no Mg^{2+}; cyan), and active PA + FtsZ (GTP + Mg^{2+}; magenta). These datasets follow a percolation-like scaling with a gel point at $\phi^* \approx 2.5\%$. A non-affine power law consistent with gelation theory[61] fits the data, $G' \approx G_0(\phi - \phi^*)^\alpha$, with best fits to Equation (1) yielding $\alpha = 3.0 \pm 0.2$ at $\phi > \phi^*$. Affine predictions ($\alpha = 1 - 1.53$) are therefore inconsistent with the experiments. In all cases the active gels exhibit lower G' than their passive counterparts, indicating internal softening from extensile filament activity. Figure 6B tracks $G'(t)$ under stationary small-amplitude oscillation. Passive matrices show slow strengthening, attributable to residual crosslinking, and GTP-free FtsZ blends remain stable.

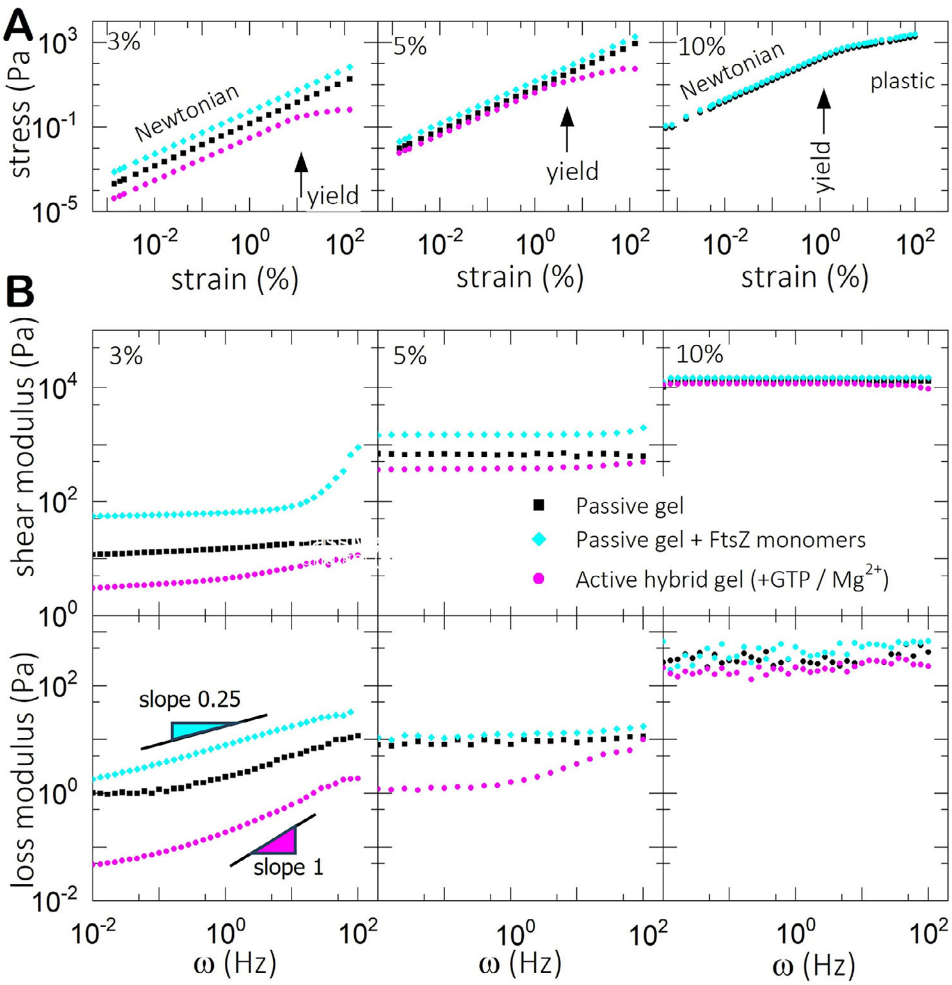

Figure 7. Rheological characterization of passive and active FtsZ–polyacrylamide hydrogels. A) Stress–strain curves for hydrogels of increasing polymer crosslinking (3%, 5%, and 10%) under oscillatory shear, showing deviations from Newtonian behavior. Passive (black) and monomeric FtsZ-blended gels (cyan) exhibit linear viscoelasticity followed by yielding and strain stiffening. In contrast, active gels containing GTP-polymerized FtsZ filaments (magenta) display nonlinear softening and, at low gel densities, plasticity-like behavior, indicating loss of mechanical integrity due to internal filament activity. B) Frequency-dependent viscoelastic moduli measured at 37 °C. Top: shear modulus (G′); bottom: loss modulus (G″). Data are shown for three PA concentrations (3%, 5%, and 10%). Active gels (magenta) exhibit pronounced frequency-dependent softening, especially at low crosslinking (3%), while passive and monomer-only systems maintain frequency-invariant behavior. The power-law scaling of G′ and G″ in active conditions is consistent with soft glassy rheology, where internal activity modulates the material's mechanical noise temperature.

In contrast, post-gelation Mg^{2+} addition to PA–FtsZ+GTP gels produces an abrupt drop in G', confirming real-time softening upon activation. Figure 6C quantifies the terminal rigidity vs FtsZ concentration, $c \equiv$ [FtsZ], for 3%, 4%, and 5% PA, concluding that softening increases monotonically with c, and is most pronounced near the percolation threshold ϕ^*, where extensile stresses propagate more effectively. Indeed, the bottom photo strip (PA + 2 mg mL^{-1} FtsZ) shows persistent tilting collapse across the same PA range, contrasting with the passive strip above, an evidence of macroscopic fluidization under self-weight. These visuals align with Figure S1 (Supporting Information), which reports G', G'', and $\tan\delta \equiv G''/G'$), under the tilt-assay settings. Small-amplitude tests give an elastic-like response for all states, either active, non-activated, or PA-only samples ($\tan\delta \ll 1$ i.e., $G' \gg G''$; see Figure S1A–C, Supporting Information), so tilt collapse is not due to viscous dominance. Rather, the tilt probes finite-stress, long-time creep: in the active state, internal extensile stresses reduce the yield stress τ_Y (see next **Figure 7A**), so the gravitational stress $\tau_G \approx \rho g H \sim 30 - 50\ Pa$ largely exceeds τ_Y, causing creep despite solid-like linear moduli ($G' > 0$). Collectively, these results establish a quantitative blueprint for tuning extensile mechanics in FtsZ-based active gels via network density and filament concentration, enabling programmable rheological responses in biohybrid soft materials.

3.7. Nonlinear Signatures Yield and Fluidization

We quantified activity-driven nonequilibrium mechanics in three formulations: passive PA, PA + FtsZ monomers (GTP-free), and active PA + FtsZ (post-gelation GTP/Mg^{2+}), rheologically analyzed across PA contents of 3%, 5%, and 10% at fixed crosslinker

(0.075%). Figure 7A (strain sweeps) shows that all samples are linear-elastic at small strain; with increasing strain, yield emerges in every case but shifts to lower strain for active gels, most prominently at 3% PA, followed by a rapid transition toward plastic flow without strain-stiffening. Passive and monomer-doped controls yield more gradually, indicating that treadmilling extensile activity nonlinearly weakens the network more effectively than passive counterparts. Figure 7B (frequency sweeps, 37 °C) reports linear shear rigidity G', and loss modulus G'', measured via small-amplitude oscillatory shear. Passive gels display classic solid-like spectra with $G' > G''$, weak dispersion in $G'(\sim \omega^0)$, and $G'' \sim \omega^{0.25}$, consistent with slow soft-glassy dissipation.[36] In contrast, active gels soften markedly: G' decreases and G'' steepens (up to $G'' \sim \omega^{0.75}$), especially at low polymer density (3% PA), hence reflecting enhanced fluidity driven by internal energy injection rather than equilibrium relaxation. Importantly, the linear response remains viscoelastic with memory (non-Newtonian), consistent with an active SGR-type regime. Across composition, higher PA content stiffens all samples, yet active gels remain significantly softer than passive counterparts, demonstrating an activity-controlled crossover from solid-like to more fluid-like behavior and highlighting how internal polymerization forces can override structural reinforcement.

3.8. Mechanical Permittivity Non-Reciprocal Susceptibility

As defined in Equation (2), we normalize the measured modulus to the Flory–Rehner (FR) passive baseline $G_0(\phi)$ (derivation/fits in Note N1, Supporting Information). Hence, we write the mechanical permittivity $\epsilon = G/G_0 = 1 + \chi$, where χ is a signed susceptibility that encodes the gel's internal reactivity to applied strain: $\chi > 0$ implies contractile stiffening ($\epsilon > 1$); $\chi < 0$ leads to extensile softening ($0 < \epsilon < 1$), with stability requiring $\chi > -1$ (thus $\epsilon > 0$). At the stress level, we use a polarization-like decomposition for effective stress (see Note N2, Supporting Information):

$$\sigma_{ij}^{(eff)} = \sigma_{ij}^{(ext)} - \sigma_{ij}^{(act)},\ \sigma_{ij}^{(int)} = \chi\,(\Gamma;\omega,\gamma)\,\sigma_{ij}^{(ext)} \tag{4}$$

which mirrors dielectric constitutive laws,[38] providing a compact, quantitative measure of internal reactivity. The Landau layer introduces a primary activity order parameter Γ (reflecting treadmilling/active stress), showing that $\chi(\Gamma;\ \omega, \gamma)$ is the secondary, signed susceptibility (Note N2, Supporting Information): for extensile activity, $\Gamma > 0$, the Landau's repulsive phase transition drives reactivity, $\chi < 0$; for contractile activity, $\Gamma < 0$, attractive interactions undergo compaction, $\chi > 0$ (mapping of susceptibility χ to activity Γ and strain γ from Note N2 (Supporting Information); FR normalization from Equations SN1–SN15 in Note N1, Supporting Information; here Equation (1)). Near onset, the Landau expansion yields a linear susceptibility–order-parameter link, $\chi(\Gamma) \approx -\chi_1\Gamma$ (mean-field), with Γ set by the stationarity condition of the Landau potential, $\alpha(\phi, \omega, \gamma)\Gamma + \beta\Gamma = 0$, which implies two solutions either $\Gamma = 0$ (no interaction, FR baseline), or $\Gamma = -\alpha/\beta$ (interactions), so that the sign of α selects the stiffening ($\chi > 0$ for $\Gamma < 0$) or softening ($\chi < 0$ for $\Gamma > 0$) branch (Note N2, Supporting Information).

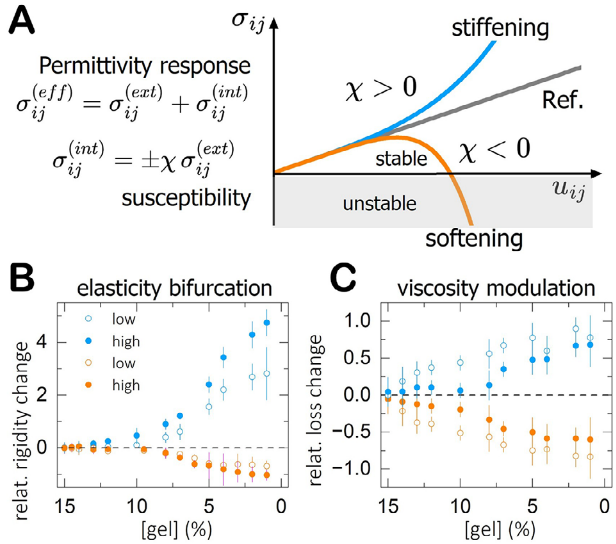

Figure 8. Mechanical bifurcation in passive and active FtsZ–PA hydrogels (fixed [FtsZ] = 2 mg mL^{-1}). A) Schematic of the susceptibility-based permittivity model (Notes N1 and N2, Supporting Information). The effective stress decomposes as $\sigma_{ij}^{(eff)} = \sigma_{ij}^{(ext)} + \sigma_{ij}^{(int)}$ with $\sigma_{ij}^{(int)} = \pm\chi\sigma_{ij}^{(ext)}$, where χ is the frequency-dependent mechanical susceptibility. Positive susceptibility ($\chi > 0$) leads to passive stiffening (upper branch), while negative susceptibility ($\chi < 0$) leads to active extensile softening (lower branch), bifurcating from the reference Flory-Rehner line ($\chi = 0$, grey). The softening branch is stable while $\epsilon = 1 \pm \chi > 0$; as $\epsilon \to 0$ the response becomes marginal and approaches instability (shaded region). B) Relative rigidity modulation ($\chi = \Delta G'/G'_0$) vs gel concentration for low- and high-frequency windows. Passive gels (blue) stiffen with PA content, whereas active gels soften (orange), most strongly at 3–5% PA. Magnitudes increase at higher frequency. C) Relative loss modulation ($\varphi = \Delta G''/G''_0$), shows the same concentration trend: passive gels exhibit larger G'' with PA content, while active gels reduce effective losses, consistent with activity-driven fluidization and internal energy injection. Error bars: s.d. over independent repeats.

Figure 8A sketches the resulting bifurcation: the passive reference ($\chi_{FR} = 0$) is linear-elastic; increasing Γ selects either an upward (stiffening) branch for $\chi > \chi_{FR}$, or a softening branch for $\chi < \chi_{FR}$, which remains stable while $\epsilon > 0$, becoming marginal/unstable as $\epsilon \to 0$ (yield). In this framework, yielding corresponds to the Landau condition where the softening branch drives instability, $\epsilon_Y = 1 + \chi_Y \to 0$ (i.e., $\chi_Y \to -1$). The branch conditions, stability, and yield criterion (γ_Y) follow from the Landau analysis in Note N2 (Supporting Information). To analyze experimental data, we report FR-referenced susceptibility changes, $\chi = \Delta G'_0/G'_0 = (G'_{FtsZ} - G'_0)/G'_0 = \epsilon - 1$, whose low-frequency limit ($\omega \to 0$) corresponds to the quasi-static, near-equilibrium deviation from the FR baseline defined in Note N1 (Supporting Information). Figure 8B (elastic modulation) shows a concentration-dependent bifurcation: passive formulations give positive susceptibility to applied stress ($\chi > 0$) with increasing PA (expected elastic reinforcement), whereas active gels exhibit internal reactance as a negative susceptibility ($\chi < 0$), most strongly at 3–5% PA, consistent with extensile softening when the network is compliant. For concise quantification, we estimate the Landau order parameter using the direct map $\Gamma_{eq} = sign\ (\chi)\sqrt{|\chi|}$ (at $\omega \to 0$, and $\gamma \to 0$) (see "Practical evaluation of

Γ" in Note N2, Supporting Information). A more accurate alternative is a full Landau inversion, fitting the stationarity condition to strain-dependent data to recover $\Gamma(\gamma)$ at the yield crossover (χ_Y). Figure 8C (loss modulation) shows the corresponding viscous response, $\varphi = \Delta G_0''/G_0'' = (G_{FtsZ}'' - G_0'')/G_0''$: passive gels trend to $\varphi > 0$ with PA content, while active gels display $\varphi < 0$ over the same range, indicating a shift toward a more fluidized, actively remodeled state. Both χ and φ display systematic frequency dependences (larger magnitudes at higher ω), consistent with a reactive contribution that grows when deformation outruns structural reorganization; the frequency-resolved form of $\chi(\omega)$ and causal Landau constraints are treated in Note N2 (Supporting Information) (with FR normalization from Note N1, Supporting Information; the SGR dispersive dressing appears in Note N3, Supporting Information). In sum, the results in Figure 8 establishes an FR-normalized, polarization-based description in which the Landau's order parameter,[40] Γ, controls the signed susceptibility $\chi(\Gamma, \gamma, \omega)$, thereby programming whether the gel stiffens (for $\chi > \chi_{FR} = 0$) or softens (for $\chi < \chi_{FR} = 0$), and setting the yield/bifurcation boundary at $\epsilon = 0$ (for $\chi = -1$). This framework rationalizes the observed composition and frequency/strain trends in active FtsZ–PA gels.

3.9. Active Viscoelastic Compliance Effective Temperature

We quantify activity-induced rheology with the complex mechanical permittivity $\tilde{\epsilon}(\gamma, \omega) = \tilde{G}/\tilde{G}_0$ (see Equation (2)), which represents the frequency- and strain-dependent mechanical compliance of the FtsZ–PA hybrid gel (Notes N2 and N3, Supporting Information), normalized to its passive PA (FR–) baseline (Note N1, Supporting Information). To disentangle activity compliance from passive swelling, we analyze $\tilde{\epsilon}(\gamma, \omega)$ throughout; depressions with respect to the FR–baseline mark activity-driven softening, whereas marginal values indicate FR-consistent passive dilution induced by swelling. **Figure** 9A reports the mechanical permittivity, $\epsilon'(\omega)$, which reflects elastic compliance. In all passive gels (3–10% PA), it remains higher than unity and weakly dispersive ($\epsilon' = 1 + \chi > 1$). Mg^{2+}/GTP activation depresses ϵ' below unity, most prominently at low PA (3%) and high frequencies, signaling activity-driven softening as imposed rates outrun structural reorganization. As anticipated by the SGR frequency dressing in Equation (3), the FR baseline $\tilde{G}_0$ is multiplied by an SGR kernel characterized by the effective noise temperature x, and structural time τ, which yields the observed frequency dispersion. The curves are well fit by the SGR–Landau model (Equation S30 in Note N3, Supporting Information; here Equation (5)):

$$\epsilon'(\omega, x) = \epsilon_0 \frac{1 + (\omega\tau)^2}{1 + (\omega\tau)^{2x}} \tag{5}$$

where ϵ_0 is the FR-normalized low-frequency plateau, τ is a structural relaxation time, and x the effective noise temperature of the SGR kernel. Asymptotically, the model yields $\epsilon' \to \epsilon_0$ for $\omega\tau \ll 1$, and $\epsilon' \approx \epsilon_0 \omega^{2-2x}$ for $\omega\tau \gg 1$: with $0 < x < 1$ (glassy/solid-like) → weak increase with ω; $x = 1$ (Maxwell-like crossover is flat at FR baseline) → frequency-independent; $x > 1$ (fluid-like regime) → decrease with ω (rate-strengthened softening). Best-fit curves to Equation (5) (solid lines) give $x < 1$ for passive gels and $x > 1$ for activated gels (strongest at 3% PA), consistent with activity elevating x and driving the system onto the extensile, fluid-like branch ($\chi < 0$, hence $\epsilon < 1$). Best-fit effective noise temperature obtained from Equation (5) are compiled in Figure S2 (Supporting Information), showing passive gels in the glassy regime ($0 < x < 1$) and Mg^{2+}/GTP-activated gels shifted to $x \geq 1$ (Maxwell-like to fluid-like), with x increasing as activity rises (Landau order parameter Γ drops).

Figure 9B reports the relative fluidity $\varphi(\omega) \equiv \omega/\epsilon''$: all samples gain fluidity with frequency, but activated gels exhibit a much steeper rise, reaching orders-of-magnitude higher φ, above 10 Hz, consistent with internal energy injection by treadmilling filaments (Note N2, Supporting Information). Remarkably, the observed trends in fluidity are well captured by the SGR–Landau expression derived (Equation S32 in Note N3, Supporting Information; here Equation (6)).

$$\varphi(\omega, x) = \frac{\omega\left[1 + (\omega\tau)^{2x}\right]}{\varphi_0\left[1 + (\omega\tau)^{2x}\right] + \epsilon_0\left[(\omega\tau)^{2-x} - (\omega\tau)^{x}\right]} \tag{6}$$

where ϵ'' is the imaginary permittivity, φ_0 is the low-frequency relative-fluidity baseline, and ϵ_0, τ and x are as above. Equation (6) reproduces the observed plateau-to-power-law crossover and the much steeper rise of $\varphi(\omega, x)$ under activation. In the glassy regime $0 < x < 1$ (passive glassy gels), φ grows modestly with ω; near the Maxwell point $x = 1$ it is weakly dispersive; for fluid-like $x > 1$ (activated gels), it increases strongly with frequency, consistent with internal energy injection by treadmilling filaments. Therefore, at fixed composition, Mg^{2+}/GTP activation drives $\epsilon' < 1$ and elevates $\varphi(\omega, x)$, evidencing softening beyond swelling with an activity-controlled high effective temperature ($x > 1$), evidencing active softening beyond swelling (i.e., $\chi < 0$ from $\Gamma > 0$). Crucially, the same parameter set (ϵ_0, τ, x) that fits $\epsilon'(\omega)$ also fits $\varphi(\omega)$, demonstrating internal consistency between the real and imaginary sectors of the mechanical permitivity $\epsilon(\omega)$, reinforcing the SGR–Landau description of active viscoelastic compliance.

Figure 9C shows the experimental correlation between the effective SGR temperature (x) and the Landau order parameter (Γ). The parameter x was obtained by fitting $\epsilon'(\omega)$ to Equation (5), while Γ is evaluated by the direct method from the measured susceptibility, $\Gamma_{eq} = sign(\chi)\sqrt{|\chi|}$, obtained from the permitivitty modulus extrapolated at zero frequency as $\chi = \epsilon - 1$. (see Notes N2 and N3, Supporting Information). The data resolve two regimes: passive gels cluster in the glassy domain $0 < x < 1$ with $\chi > 0$ (contractile, ordered states, $\Gamma_{eq} > 0$), whereas Mg^{2+}/GTP-activated gels shift into the fluid-like domain $x \geq 1$ with $\chi < 0$ (extensile activity, $\Gamma_{eq} < 0$). Thus, FtsZ treadmilling elevates the thermal-like drivin force (through x) and flips the sign of the internal susceptibility ($\pm\chi$). This glassy→fluid crossover is the Landau-type bifurcation (Figure 8; Note SN2, Supporting Information), where the primary structural parameter, $\Gamma_{eq} > 0$, governs the secondary rheological response, $\chi(\Gamma, \omega)$, selecting either stiffening ($\chi > 0$) or softening ($\chi < 0$). These results consolidate the SGR–Landau picture of active viscoelastic compliance: internal filament dynamics act as a thermal-like source that renormalizes the mechanical permittivity to sub-unitary values ($\epsilon < 1$) and sets a negative, non-reciprocal susceptibility ($\chi < 0$).

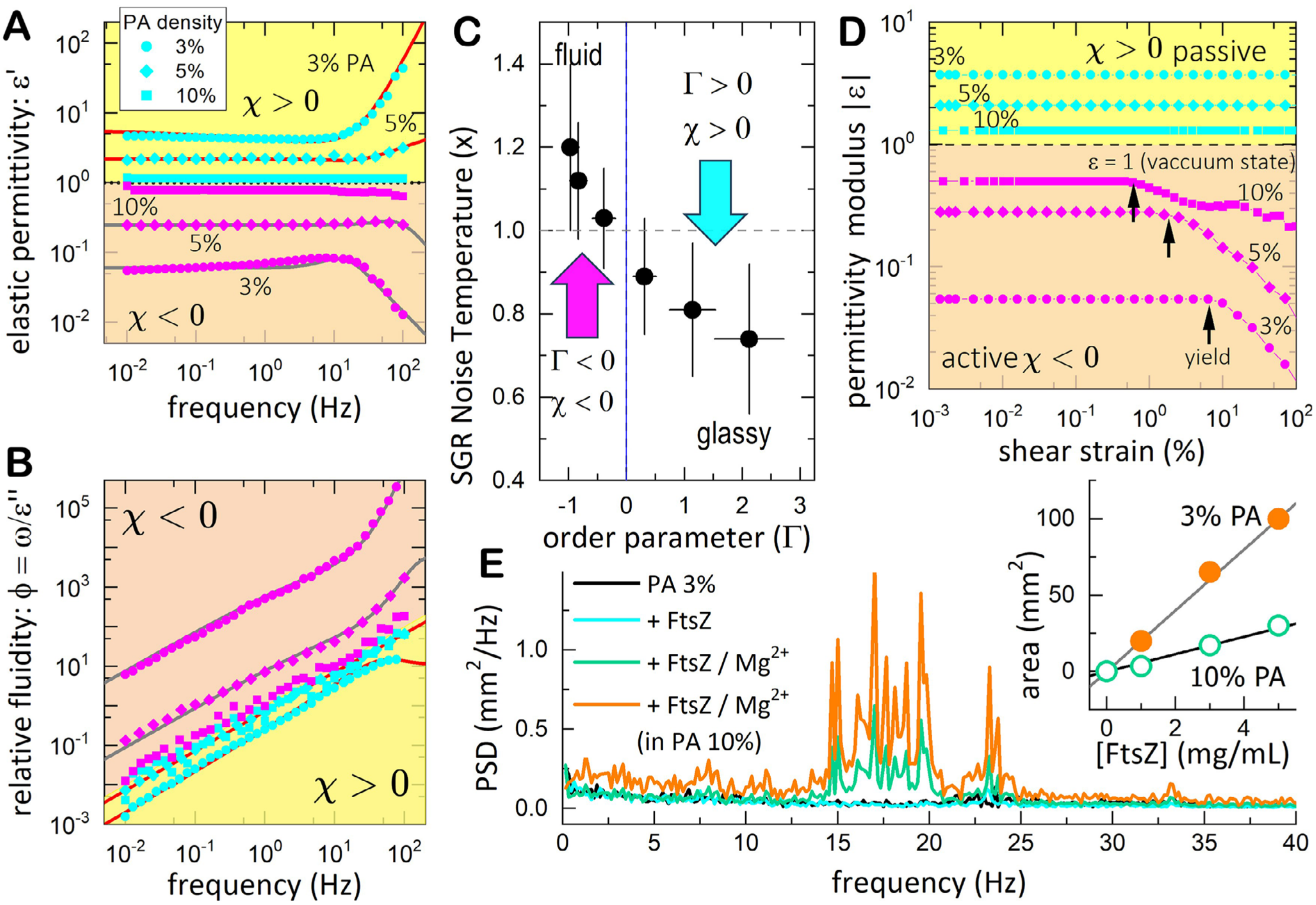

Figure 9. Viscoelastic response of hybrid FtsZ–PA hydrogels under internal force generation. A) Elastic permittivity vs frequency for hybrid gels (fixed [FtsZ] = 2 mg mL^{-1}) at different PA densities (symbols: 3%, 5%, and 10%). Straight lines are best fits to SGR permitivity in Equation (5) (see Note N3, Supporting Information). Passive gels (χ>0) show a constant plateau, while activated gels (χ<0) display a frequency-dependent softening above 1 Hz, consistent with internally driven reactive compliance. B) Relative fluidity ($\phi = \omega/\epsilon''$) increases with frequency and activity, showing enhanced dissipative response at high deformation rates (symbols as in A; solid lines: fits to SGR fluidity in Equation (6) (see Note N3, Supporting Information). C) Experimental correlation between the effective SGR noise temperature (x) and the Landau order parameter (Γ), extracted from fits to Equation (5) (see Figure S2, and Note N3, Supporting Information). Passive gels occupy the glassy domain (x < 1) corresponding to contractile, ordered states ($\Gamma > 0$, thus $\chi > 0$), while Mg^{2+}/GTP activation shifts the system into the fluid-like domain (x > 1), characteristic of extensile, disordered activity ($\Gamma < 0$, thus $\chi < 0$). The upward (magenta) and downward (cyan) arrows mark the direction of active transitions between these mechanical phases, indicating how FtsZ treadmilling elevates the effective mechanical temperature driving the Landau bifurcation (see Note N2, Supporting Information). D) Permittivity modulus (ϵ) vs strain reveals a transition from passive, elastic behavior ($\epsilon > 1$) to active softening ($\epsilon < 1$ as activity grows. The yield point (arrows) shifts to higher strain, marking a Landau-type bifurcation between stable and marginal states under increased deformation (see Note N2, Supporting Information). E) Laser Doppler vibrometry (LDV) spectra of hybrid gels show distinct hydrodynamic modes arising from active FtsZ treadmilling. Activation (GTP + Mg^{2+}) in PA hydrogels (7% density, 2.5% crosslinking, [FtsZ] = 5 mg mL^{-1}) produces strong peaks corresponding to internally driven oscillations. Inset: LDV amplitude (integrated area) increases with [FtsZ] but decreases with PA density, indicating that softer matrices more effectively transmit active mechanical noise.

Figure 9D shows the strain-dependent modulus $|\epsilon(\gamma)|$: passive gels are strain-invariant, while activated gels display strain-softening with a yield crossover at $\gamma_Y \approx 1 - 10\%$, (strongest at 3% PA); crossing from $|\epsilon| \approx 1$ —the FR "mechanical vacuum", to $|\epsilon| < 1$, corresponding to leaving the passive branch, entering the extensible branch predicted by the Landau susceptibility model, with the approach to $|\epsilon| \to 0$ marking the bifurcation/yield boundary (Note N2, Supporting Information). The strain-dependent decrease of $\epsilon(\gamma)$ rationalizes the tilt-collapse exihibited by active gels (see Figure 6), where self-weight exceeds the lowered τ_Y ($\ll \gamma_G \approx \rho g H$), despite finite shear rigidity ($G' > 0$).

Figure 9E shows laser-Doppler spectra with distinct PSD peaks (≈15, 17, 19.5, and 23.5 Hz, within the 0–40 Hz acoustic band), appearing only in activated, low-PA gels (3%), revealing active hydrodynamic modes that underpin the high-frequency rise in fluidity φ, and the drop in permittivity ϵ'. Taken together, these data demonstrate that FtsZ activation converts the gel into a rate- and strain-programmable extensile metamaterial: the FR– baseline separates dilution from activity, the Landau layer links the signed susceptibility and yield, and the SGR dressing accounts for the frequency dependence, providing a compact, predictive description of the active viscoelastic compliance.

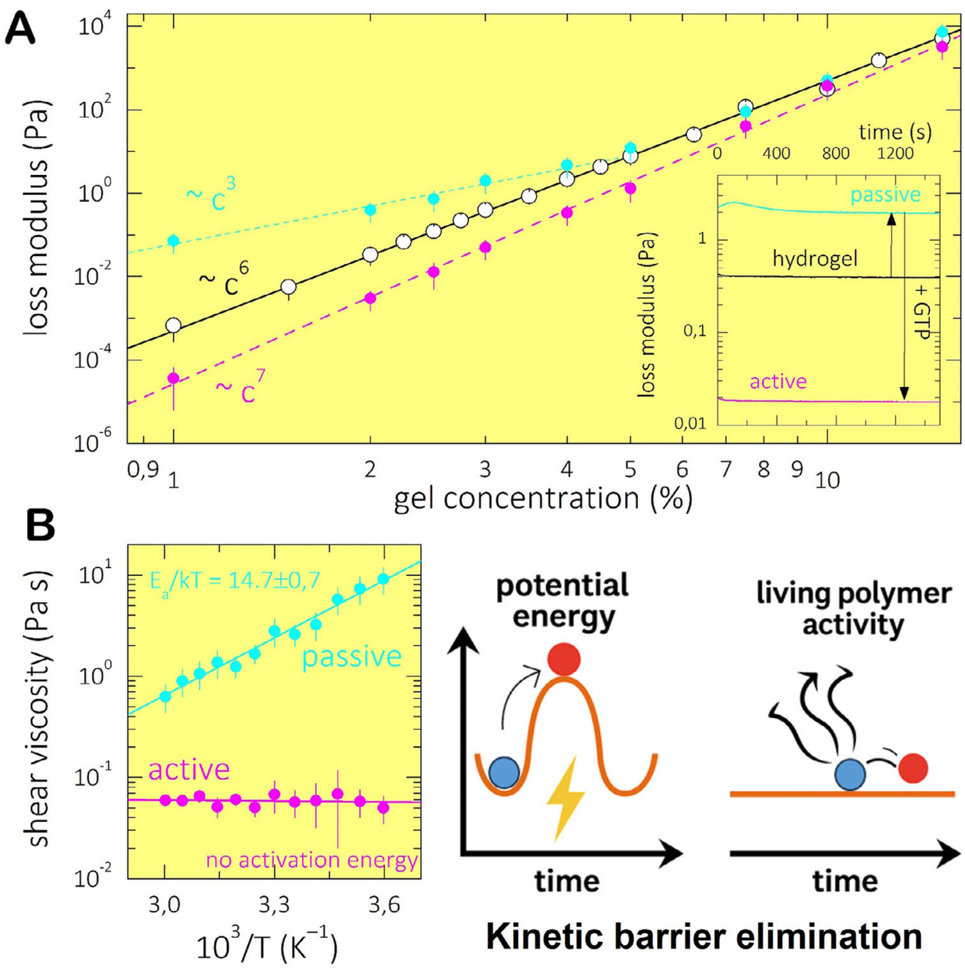

Figure 10. Concentration and temperature dependences of viscous dissipation in FtsZ–PA gels. A) Loss modulus (G'') vs acrylamide concentration for FtsZ-free PA (black), passive hybrids (PA + FtsZ, no GTP; cyan), and active hybrids (PA + FtsZ + GTP/Mg^{2+}; magenta). Solid lines are power-law fits over the plotted range: $G''_0 \sim \phi^6$ (black), $G''_{pass} \sim \phi^3$ (cyan) and $G''_{act} \sim \phi^7$ (magenta). The active state shows the steepest concentration scaling, consistent with additional dissipation arising from internally generated stresses by living polymers beyond classical entanglement. Inset: at 3.5% PA, $G''(t)$ drops abruptly upon GTP addition (arrow), indicating activation-driven fluidization. B) Arrhenius plots of shear viscosity at 3.5% PA. Passive gels show Arrhenius behavior (Equation (7)), yielding an activation energy of $E_a/k_BT = 14.7 \pm 0.7$, evidencing a thermal barrier for flow. Active gels display no measurable temperature dependence over the same range (flat trend), consistent with barrier elimination by internal FtsZ treadmilling. Schematic (right): in the passive state, motion requires thermal activation over an energy barrier; upon activation, internally generated stresses flatten the barrier, enabling drift-like flow without thermal assistance.

3.10. The Hybrid FtsZ-PA Gel is Hyperfluid

Figure 10 quantifies how activation reshapes dissipation. In Figure 10A, the loss modulus, G'', scales steeply with polymer density (ϕ), both for passive PA networks, and for PA doped with FtsZ monomers (no GTP), following $G'' \sim \phi^{\delta}$, with scaling exponent $\delta_{pass} = 6.1 \pm 0.2$, consistent with entanglement-controlled dissipation in percolating networks.[20] Upon Mg^{2+}/GTP activation, the scaling dependence weakens stronlgly to $\delta_{act} = 2.8 \pm 0.3$, revealing concentration-sensitive fluidization that is most pronounced in compliant matrices; at fixed ϕ (3.5%), introducing

GTP/Mg^{2+} produces an abrupt drop in G'' (inset), marking the onset of treadmilling and internally generated extensile stress leading to fluidization.

3.11. Activation Eliminates Thermal Flow Barriers

Figure 10B examines the temperature dependence of flow resistance. Passive gels display Arrhenius-type behavior:

$$\eta = \eta_0 e^{-E_a/k_BT}. \tag{7}$$

with an extracted activation energy $E_a^P/k_BT = 14.7 \pm 0.7$, indicating a thermal barrier for network rearrangement. Activated gels, by contrast, show no measurable temperature dependence over the same range ($E_a^A \approx 0$), evidencing collapse of that barrier: non-thermal work supplied by treadmilling filaments supplants thermally assisted relaxation, consistent with the large burst energies inferred, $E_\xi \approx 10^3 k_BT \gg E_a^P \gg E_a^A$ (see Figure 3). Taken together, the decreased scaling of viscous losses, $G''(\phi) = \omega\eta$, and temperature-independent viscosity η, establish an actively softened regime ($\epsilon < 1$), with an enhanced hyperfluidity ($\varphi \to 0$), in which flow is governed by endogenous stress generation rather than by thermal agitation. Living FtsZ activation thus biochemically programs a barrier-free, internally driven reduction of mechanical impedance within the PA hydrogel matrix.

4. Discussion

This work is a proof-of-concept performed in a deliberately highly hydrated hydrogel, chosen to preserve ample interstitial space so that treadmilling FtsZ filaments can operate and transmit extensile stress. Accordingly, the low–polymer-density formulations are not intended to be load-bearing but to serve as permissive matrices that reveal biochemical-to-mechanical transduction with high sensitivity. Unlike processive, polarity-guided eukaryotic actin/ tubulin systems that typically generate contractile stresses by pulling along persistent tracks,[8,62] bacterial FtsZ assembles into short, dynamic "living" filaments that reorganize stochastically and act as rotating force dipoles capable of exerting extensile stresses away from their center of mass.[48] Two observations support intragel retention of FtsZ over experimental time scales: i) activation-induced softening persists for hours until GTP exhaustion without drifting back to baseline; and ii) mesh-size estimates (tens of nanometers) are smaller than the hydrodynamic dimensions of FtsZ filaments/bundles, providing a physical barrier to egress. Thus, the observed mechanical remodeling arises from retained, internal FtsZ activity within a stable, hydrated scaffold. The resulting living-polymer activity dilates and fluidizes the embedding gel.

The hybrid response depends on two structural factors: i) the tribological interaction between active filaments and the matrix cavities, which governs force transmission under contact; and ii) the network connectivity, which controls the spatial coherence of stress propagation. The measured reductions in viscoelastic moduli, mechanical permittivity, yield stress, and the collapse of the Arrhenius activation barrier together point to a hyperfluid active state, in which dissipation and flow are dominated by internally generated forces rather than thermally activated rearrangements. Soft active hydrogels formed by polymerizing protein filaments are widespread in nature, notably in cytoskeletal assemblies and extracellular matrices, where they support protection, mechanosensing and remodeling.

Our permittivity framework, $\epsilon(\omega, \gamma) = G/G_0 = 1 + \chi$, admits a direct analogy to dielectric permittivity in resonant metamaterials: in plasmonic/acoustic media, field–matter coupling produces negative susceptibility and near-resonant amplification by drawing energy from an internal reservoir. Here, extensile activity plays the role of internal gain: it reduces effective dissipation and drives the system toward a soft mode where $\chi < 0 \Rightarrow \epsilon < 1$, yielding hyperfluid amplification of imposed strain (enhanced creep/flow at finite stress) while the small-amplitude response remains solid-like ($G' > G''$). The two experimental control axes, i.e., frequency (broad SGR-type spectra) and strain (Landau yield crossover), map onto dispersion and nonlinear susceptibility in active metamaterials. In this view, the tilt-assay collapse corresponds to operating near a mechanically amplified state with internal gain, where self-weight is effectively amplified by activity faster than it can be elastically restored, producing macroscopic flow despite finite shear rigidity ($G' > 0$). This analogy reframes mechanical reactivity ($\epsilon < 1$) as active amplification due to resonant acoustic modes, rather than mere dilution, suggesting targeted protocols to further probe nonlinear mechanisms "mechanical resonance" (e.g., frequency sweeps under weak prestrain, or ion/light-modulated activity to tune the gain).

Conceptually, we embed the bacterial, self-assembling cytoskeletal protein FtsZ into a compliant polymer network. Upon GTP activation, FtsZ treadmills and converts chemical free energy into localized mechanical work, driving the composite far from equilibrium. This design principle—incorporating self-assembling, force-generating proteins into soft matrices, echoes strategies found in natural soft matter, which regulate cytokinetic fluidity and self-healing in hydrogels,[63] muscular hydrostat function,[64] and reactive elasticity underlying nastic/tropic plant motions.[65,66] In our work, polyacrylamide (PA) was selected as the matrix for its biocompatibility, ease of functionalization, and well-characterized mechanics, allowing us to isolate FtsZ-driven effects; its relative chemical inertness minimizes unintended interactions with FtsZ.

Within a synthetic-biology perspective, these results motivate a class of active microgels composed of living FtsZ polymers embedded in polymer matrices. Stiffness gradients, matrix connectivity, and the spatial distribution of activity together will dictate emergent mechanics. While PA is ideal for deconvolving mechanisms, it is not optimized for biomedical translation. Future iterations can employ mesh-preserving reinforcement (double networks; reformable supramolecular linkages) to elevate moduli without sacrificing interstitial space, and explore biodegradable or bioactive scaffolds (alginate, agarose, collagen, GelMA, etc.) to broaden function. Such materials could enable reconfigurable soft actuators, stress-sensing substrates, and morphable microenvironments whose viscoelastic state is programmed biochemically by internal living-polymer dynamics.

4.1. Positioning Relative to Existing Active Gel Systems

Active-gel platforms built from actomyosin or microtubule–kinesin typically display contractile behavior that raises stiffness and transmits tension over distance. By contrast, the FtsZ–PA hybrids presented here are extensile: activation lowers viscoelastic moduli and yield, suppresses the Arrhenius flow barrier, and promotes fluidization rather than reinforcement. This softening arises from pushing stress generated by treadmilling FtsZ that locally reorganizes the matrix, aligning more closely with biological softening used in morphogenesis and cell migration than with long-range tensioning. Practically, FtsZ offers a simple, robust route to tunable extensile stresses without elaborate filament alignment or motor crosslinking; its bacterial origin supports scalable production, and its reversible, self-limiting polymerization affords dynamic control of the active state.

4.2. Modularity Toward Functional Architectures

The microgel formulation enables modular assembly of higher-order structures with spatially patterned stiffness gradients, asymmetric responses, or localized activation, features central to soft machines and adaptive interfaces. We envision arrays of FtsZ–PA microgels coupled to stimulus-responsive control layers (e.g., ion/light gating) to implement mechanical "logic" such as switching or thresholding. The underlying extensile mechanics naturally support non-reciprocal behaviors, e.g., distinct loading vs relaxation pathways, providing a complementary modality to contractile platforms and broadening the functional design space for programmable, living-polymer materials.

5. Conclusion

We created an extensible active hydrogel by embedding living FtsZ polymers in polyacrylamide: Mg^{2+}/GTP activation drives isotropic swelling and pronounced softening/fluidization. These behaviors are quantitatively captured by an FR–Landau–SGR framework that separates passive dilution from genuine activity, consistent across swelling, rheology, and microrheology. Our principal achievements translate directly into two immediate avenues for application and validation. First, establishing reversible on/off control will test causality between treadmilling and softening and enable cyclic operation. Second, mesh-preserving reinforcement and spatial patterning will convert the extensile response into programmable architectures for biomedical and soft-robotic functions.

5.1. Toward Reversible Cycling

Achieving uniform on/off control in bulk gels is challenging because Mg^{2+} both initiates treadmilling and is difficult to remove homogeneously. We will implement i) microfluidic perfusion to rapidly switch between Mg^{2+}/GTP and low-Mg^{2+}/GTP-free buffers, and ii) spatiotemporal cofactor control using photo-caged Mg^{2+}, caged chelators, or caged GTP for reversible, uniform switching. To decouple assembly from dynamics-driven softening, non-hydrolyzable GTP analogs (GMPCPP/GMPPNP + Mg^{2+}) will provide assembly without treadmilling, preserving the FR baseline and rigorously testing the requirement of turnover. These tools enable quantitative hysteresis and reversibility assays over multiple cycles.

5.2. Programmable Active Soft Matter

With cycling in place, FtsZ–PA hybrids become internally actuated materials whose viscoelastic state is set from within. By tuning matrix connectivity and the spatial distribution of active filaments, we can program stiffness, yield, and dissipation on demand. To raise rigidity without sacrificing the permissive mesh that sustains activity, we will employ mesh-preserving reinforcement via double-network architectures and reformable supramolecular linkages. This paves a modular route to biomimetic extensile metamaterials for tissue engineering, adaptive biomaterials, and soft robotic actuators.

6. Experimental Section

Preparation of FtsZ–Polyacrylamide Hybrid Hydrogels: Recombinant *Escherichia coli* FtsZ protein was purified as described previously and stored at −80 °C in a GTP-free buffer. Hybrid hydrogels were prepared by co-polymerizing FtsZ within an acrylamide/bis-acrylamide network. The prepolymer solution contained acrylamide (2.5–10% w v^{-1}), N,N′-methylenebisacrylamide (0.07% w v^{-1}), 0.5 mg Ml^{-1} FtsZ, and 1 mM GTP in a buffer composed of 50 mM HEPES, 100 mM KCl, pH 7.5. Polymerization was initiated by adding 0.05% ammonium persulfate (APS) and 0.05% TEMED under isotonic conditions. To prevent premature FtsZ activation, no Mg^{2+} was present during polymerization. Gels were cast in flat or cylindrical geometries depending on the intended analysis (microscopy, rheology, or swelling assays).

System and Activation: Control Conditions: Hybrid PA–FtsZ hydrogels were equilibrated overnight at 4 °C in polymerization buffer containing GTP but no Mg^{2+}. Activation was always post-gelation by transferring the same specimens to fresh buffer with 2 mM $MgCl_2$ at 37 °C (unless stated otherwise). Controls: i) PA–FtsZ without GTP (monomeric FtsZ), ii) PA-only, iii) PA–FtsZ+GTP in Mg^{2+}-free buffer (non-activated), and iv) isotonic ionic control (3 mM KCl, osmolarity matched to 2 mM $MgCl_2$). FtsZ was not chemically coupled to PA; the protein was physically entrapped during PA gelation. Upon Mg^{2+} addition, GTP-bound FtsZ polymerized and treadmilled, forming living filaments that interpenetrated the crosslinked PA network without covalent linkage.

Microgel Droplet Formation: Swelling Essay: Microscale gel droplets (≈100 µm diameter) were fabricated using a millifluidic injection setup composed of a fine-tipped glass capillary connected to a syringe pump. Droplets were polymerized directly into an isotonic aqueous bath containing acrylamide monomers, photoinitiators and cross-linkers mixed with FtsZ and GTP (Mg^{2+} omitted), followed by overnight incubation to ensure completion of gelation and passive swelling equilibrium under hybrid polymerization. Bright-field microscopy (Nikon TE2000, 4 × and 10 × objectives) was used to image individual microgels after this first equilibration. FtsZ activation was then triggered by addition of Mg^{2+}, and the samples were further incubated until a second post-activation swelling equilibrium was reached after 1 h. Quantification of radius and volume changes between the two equilibrium states (pre- and post-activation) was performed using image segmentation and circular contour fitting in ImageJ.

Scanning Electron Microscopy (SEM): Polyacrylamide gels (2.5% and 7% PA) were prepared either as bare PA controls or as hybrid PA–FtsZ composites. For hybrid gels, recombinant FtsZ (final 2 mg mL^{-1}) was mixed into the acrylamide/bisacrylamide precursor solution before gelation. After gelation, hybrid gels were equilibrated in GTP-containing buffer (1 mM GTP; no Mg^{2+}) for 30–60 min to obtain GTP-bound, non-treadmilling FtsZ assemblies prior to fixation. SEM samples were prepared with GTP (no Mg^{2+}) to embed passive, non-treadmilling filaments, ensuring that living dynamics do not confound ultrastructure. All samples were then processed identically: fixation in 2% (v v^{-1}) glutaraldehyde in PBS (pH 7.4) for 30–60 min at room temperature, brief PBS rinse, post-fixation in 1% (w v^{-1}) osmium tetroxide for 30 min at 4 °C, and thorough rinsing. Dehydration was carried out through a graded ethanol series (30%, 50%, 70%, 90%, 96%, and 100%; 10–15 min each). No freezing steps were used. Gels were dried by CO_2 critical-point drying to preserve the porous microstructure, mounted on aluminum stubs using conductive carbon tape, and sputter-coated with ≈5–8 nm Au Pd. Imaging was performed on a Hitachi TM-1000 tabletop SEM operated at 15 kV in high-vacuum mode. For each condition, ≥3 independent gels were imaged, sampling multiple fields (typical magnifications 500×); scale bars are indicated in the figure panels. Samples were CO_2 critical-point dried to limit drying artifacts; nevertheless, SEM depicts the dehydrated scaffold, which can exhibit micron-scale wrinkling and macro-void textures that do not correspond one-to-one to the hydrated mesh size.

Rheology Measurements: Bulk rheological characterization was performed using a stress-controlled shear rheometer (TA Instruments) in a 40 mm cone plate configuration. Gels were equilibrated at 37 °C, and G′ (shear modulus) and η (viscosity) were measured in real time before and after Mg^{2+} addition. Frequency sweeps (0.01–10 Hz) and strain sweeps (0.01%–50%) were performed to assess viscoelastic behavior across the linear and nonlinear regimes. For Arrhenius analysis, viscosity was recorded at a constant shear rate (1 s^{-1}) across temperatures from 15 to 40 °C. Each condition was run in triplicate ($n = 3$); plots show replicate averages with SD. Instrument calibration was verified; observed SD matched measurement accuracy. Datasets with replicate SD exceeding instrument accuracy at the measured signal were discarded and repeated.

Particle Tracking: For Brownian motion tracking, hydrophilic microparticles (≈1 µm diameter) were synthesized using an oil-in-water emulsion polymerization. A monomer mix composed of 60 mol% methyl methacrylate (MMA), 40 mol% poly(ethylene glycol) methacrylate (PEGMA, MW 300–500), and 0.5 mol% ethylene glycol dimethacrylate (EGDMA) was emulsified in 1% sodium dodecyl sulfate (SDS) via probe sonication. Polymerization was initiated with APS (0.5% w v^{-1}) and TEMED (0.05% v v^{-1}) under a nitrogen atmosphere at room temperature. The PEG-rich composition produced microparticles with a net density of 1.00 ± 0.01 g cm^{-3}, confirmed by sedimentation and sucrose gradient flotation assays, thus ensuring neutral buoyancy and preventing sedimentation during gel polymerization and measurement. The surface chemistry conferred by PEG also rendered the particles strongly hydrophilic and inert, minimizing non-specific adhesion or mechanical coupling to FtsZ filaments. After synthesis, particles were washed and resuspended in phosphate-buffered saline (PBS, pH 7.4) containing 0.01% Tween-20 to prevent aggregation. They were added to the FtsZ–PA pre-gel solution at a final concentration of $\approx 10^6$ particles mL^{-1} and gently mixed before casting to ensure homogeneous spatial distribution throughout the hydrogel matrix.

Synthesis of Tracking Microparticles: Carboxylated polystyrene microparticles were synthesized using a surfactant-stabilized dispersion polymerization in aqueous medium. The reaction mixture consisted of 10% (v v^{-1}) styrene monomer and 2% (w v^{-1}) acrylic acid as a comonomer to introduce surface carboxyl groups, emulsified in deionized water containing 0.5% sodium dodecyl sulfate (SDS). The emulsion was homogenized by magnetic stirring under nitrogen for 30 min to eliminate dissolved oxygen. Polymerization was initiated by addition of 0.5% ammonium persulfate (APS) at 70 °C under continuous stirring for 6 h. The resulting colloidal suspension was cooled to room temperature and centrifuged at 5000 g for 10 min. The particles were washed three times with deionized water and resuspended in phosphate-buffered saline (PBS, pH 7.4) containing 0.01% Tween-20 to prevent aggregation. Particle size and uniformity were confirmed by dynamic light scattering and optical microscopy, yielding a near monodisperse population of microparticles (1.05±0.03 µm, 0.103 PDI in diameter) with a surface density of carboxyl groups suitable for colloidal stability under physiological conditions. To ensure near-neutral buoyancy, the synthesis conditions were optimized to produce particles with a density close to water (1.03–1.05 g cm^{-3}).

Brownian Motion Analysis: The hydrophilic, carboxylated surfaces of microparticle tracers minimized non-specific interactions with FtsZ filaments, enabling reliable tracking of thermally driven and active fluctuations when embedded in the hybrid FtsZ–PA hydrogel. To probe internal force fluctuations, 1-µm carboxylated polystyrene beads were embedded in the gel prepolymer solution prior to curing. Bead motion was recorded by high-speed video microscopy (100 fps) using a sCMOS camera (Photron) under 40 × magnification in a phase contrast microscope (TE2000, Nikon). Trajectories were extracted using TrackMate (ImageJ), and displacement distributions, mean square displacements (MSD), and non-Gaussian parameters were computed to quantify deviation from equilibrium thermal diffusion.

Laser Doppler Velocimetry (LDV): To characterize the dynamic behavior of the FtsZ-PA hydrogels and quantify the FtsZ-driven hydrodynamic modes, we employed Laser Doppler Velocimetry (LDV). Measurements were performed using a LDV100 instrument (Polytec, Germany), equipped with a He—Ne (632.8 nm wavelenght) laser. The hydrogel sample was placed on the stage of the LDV instrument, and the laser beam was focused into the sample center using a focusing objective. The backscattered light from the hydrogel was collected by the same objective and directed to a photodetector. The Doppler frequency shift of the backscattered light, which is proportional to the velocity of the microparticles, was analyzed using a fast Fourier transform (FFT) to generate a power spectral density (PSD) spectrum.

Data Analysis and Statistics: All experiments were replicated at least three times. Data are presented as mean ± standard deviation unless otherwise stated. Curve fitting (power-law exponents, Arrhenius plots) and statistical analysis were performed using OriginPro and Python (SciPy). Significance of mechanical softening and volume changes was assessed using Student's t-tests, with $p < 0.05$ considered significant. For displacement probability distributions, differences between passive and active states were further evaluated using a two-sample Kolmogorov–Smirnov test (two-sided), which confirmed a statistically significant divergence ($p < 0.05$).

Supporting Information

Supporting Information is available from the Wiley Online Library or from the author.

Acknowledgements

The authors thank G. Rivas and M. Vicente for providing the purified FtsZ samples, I. López-Montero and P. Natale for assistance with hydrogels' preparation, and M. Vélez for discussions. The RSS of Instituto de Catálisis y Petroleoquímica (ICP)-CSIC, Spain is acknowledged for making SEM available for use. This research was supported by the Spanish Ministry of Science and Innovation (MICINN–Agencia Española de Investigación AEI) under grants FIS2015-70339-C2-1-R, PID2019-108391RB-100, and TED2021-132296B-C52 (to FM), TED2021-132296B-C53 (to DHA), and Comunidad de Madrid under grants S2018/NMT-4389 and Y2018/BIO-5207 (to FM). This study was also funded by the REACT-EU program PR38-21- 28 ANTICIPA-CM, a grant by Comunidad de Madrid and European Union under FEDER program, from European Union in response to COVID-19 pandemics. The funders had no role in the study design, data collection, analysis, preparation of the manuscript, or the decision to publish.

Conflict of Interest

The authors declare no conflict of interest.

Author Contributions

D.H.A. and F.M. contributed equally to this work. M.K. and C.L.R. prepared the samples, conducted the experiments, and analyzed the data, assisted by D.H.A., M.C., H.L.M, P.L., and C.S. D.H.A. designed computational tools. M.K., P.L., C.S., and F.M. conceived the experiments, prepared the figures, and drafted the manuscript. F.M. designed the research. All authors contributed to the manuscript.

Declaration of Generative AI in the Writing Process

The authors used ChatGPT (OpenAI, GPT-4) only for language polishing (grammar/clarity) of selected sentences and for drafting schematic cartoons used in the Graphical Abstract and Figure 1A/Figure 2C. The tool was not used to generate scientific content, design experiments, analyze data, develop models, or draw conclusions. All AI-assisted text and images were reviewed, edited, and approved by the authors, who take full responsibility for the final manuscript. No confidential or personal data were provided to the tool.

Data Availability Statement

The data that support the findings of this study are available from the corresponding author upon reasonable request.

Keywords

active matter, cytokinetic filaments, hydrogel, living polymers, soft robotics

Received: August 21, 2025
Revised: November 11, 2025
Published online: December 5, 2025

[1] J. Prost, F. Jülicher, J. F. Joanny, *Nat. Phys.* **2015**, *11*, 111.
[2] M. C. Marchetti, J. F. Joanny, S. Ramaswamy, T. B. Liverpool, J. Prost, M. Rao, R. A. Simha, *Rev. Mod. Phys.* **2013**, *85*, 1143.
[3] S. Ramaswamy, *Annu. Rev. Cond. Matter Phys.* **2010**, *1*, 323.
[4] J. Aizenberg, P. Fratzl, *Adv. Mater.* **2009**, *21*, 387.
[5] X. He, M. Aizenberg, O. Kuksenok, L. D. Zarzar, A. Shastri, A. C. Balazs, J. Aizenberg, *Nature* **2012**, *487*, 214.
[6] K. Liu, Y. Kang, Z. Wang, X. Zhang, *Adv. Mat.* **2013**, *25*, 5530.
[7] M. L. Gardel, J. H. Shin, F. C. MacKintosh, L. Mahadevan, P. Matsudaira, D. A. Weitz, *Science* **2004**, *304*, 1301.
[8] A. Doostmohammadi, J. Ignés-Mullol, J. M. Yeomans, F. Sagùes, *Nat. Commun.* **2018**, *9*, 3246.
[9] V. Schaller, C. Weber, C. Semmrich, E. Frey, A. R. Bausch, *Nature* **2010**, *467*, 73.
[10] G. Romet-Lemonne, C. Leduc, A. Jégou, H. Wioland, *Annu. Rev. Biophys.* **2025**, *54*, 303.
[11] B. Adhikari, M. A. Stager, M. A. Krebs, *J. Biomed. Mater. Res. A* **2023**, *111*, 660.
[12] M. Hamidi, A. Azadi, P. Rafiei, *Adv. Drug Delivery Rev.* **2008**, *60*, 1638.
[13] M. Otake, Y. Kagami, M. Inaba, H. Inoue, *Robot. Auton. Syst.* **2002**, *40*, 185.
[14] G. H. Kwon, J. Y. Park, J. Y. Kim, M. L. Frisk, D. J. Beebe, S.-H. Lee, *Small* **2008**, *4*, 2148.
[15] J. P. Gong, Y. Katsuyama, T. Kurokawa, Y. Osada, *Adv. Mat.* **2003**, *15*, 1155.
[16] L. A. Estroff, A. D. Hamilton, *Chem. Rev.* **2004**, *104*, 1201.
[17] P. Rao, T. L. Sun, L. Chen, R. Takahashi, G. Shinohara, H. Guo, D. R. King, T. Kurokawa, J. P. Gong, *Adv. Mat.* **2018**, *30*, 1801884.
[18] S. Talebian, M. Mehrali, N. Taebnia, C. P. Pennisi, F. B. Kadumudi, J. Foroughi, M. Hasany, M. Nikkhah, M. Akbari, G. Orive, A. Dolatshahi-Pirouz, *Adv. Sci.* **2019**, *6*, 1801664.
[19] X. Kuang, M. O. Arican, T. Zhou, X. Zhao, Y. S. Zhang, *Acc. Mater. Res.* **2023**, *4*, 101.
[20] J.-L. Laurent, P. A. Janmey, J. D. Ferry, *J. Rheol.* **1980**, *24*, 87.
[21] B. J. Peter, H. M. Kent, I. G. Mills, Y. Vallis, P. J. G. Butler, P. R. Evans, H. T. McMahon, *Science* **2004**, *303*, 495.
[22] H. T. McMahon, J. L. Gallop, *Nature* **2005**, *438*, 590.
[23] J. Howard, *Nature* **1997**, *389*, 561.
[24] R. Cooke, *The FASEB J.* **1995**, *9*, 636.
[25] J. Howard, A. J. Hudspeth, R. D. Vale, *Nature* **1989**, *342*, 154.
[26] D. A. Fletcher, R. D. Mullins, *Nature* **2010**, *463*, 485.
[27] M. L. Gardel, I. C. Schneider, Y. Aratyn-Schaus, C. M. Waterman, *Annu. Rev. Cell Dev. Biol.* **2010**, *26*, 315.
[28] W. Margolin, *Nat. Rev. Mol. Cell Biol.* **2005**, *6*, 862.
[29] D. M. Adams, J. Errington, *Nat. Rev. Micro.* **2009**, *7*, 642.
[30] M. Loose, T. Mitchison, *Nat. Cell Biol.* **2014**, *16*, 38.
[31] A. Mukherjee, J. Lutkenhaus, *EMBO J.* **1998**, *17*, 462.
[32] X. Yang, Z. Lyu, A. Miguel, R. McQuillen, K. C. Huang, J. Xiao, *Science* **2017**, *355*, 744.
[33] A. W. Bisson-Filho, Y.-P. Hsu, G. R. Squyres, E. Kuru, F. Wu, C. Jukes, Y. Sun, C. Dekker, S. J. Holden, M. S. VanNieuwenhze, Y. V. Brun, E. C. Garner, *Science* **2017**, *355*, 739.
[34] P. Flory, J. Rehner, *J. Chem. Phys.* **1943**, *11*, 521.
[35] M. Rubinstein, R. H. Colby, *Polymer Physics*, Oxford University Press, Oxford **2003**.
[36] T. Tanaka, *Phys. Rev. Lett.* **1978**, *40*, 820.
[37] Y. Li, T. J. Tanaka, *J. Chem. Phys.* **1989**, *90*, 5161.
[38] R. V. Craster, S. Guenneau, *Acoustic Metamaterials: Negative Refraction, Imaging, Lensing and Cloaking*, Springer, NY USA, **2013**.
[39] P. Sollich, F. Lequeux, P. Hébraud, M. E. Cates, *Phys. Rev. Lett.* **1997**, *78*, 2020.
[40] H. López-Menéndez, C. Luque-Rioja, M. Kharbedia, D. Herráez-Aguilar, J. A. Santiago, F. Monroy, *Soft Matter.* **2025**, *21*, 670.
[41] G. Gomper, H. A. Stone, C. Kurzthaler, D. Saintillan, F. Peruani, D. A. Fedosov, T. Auth, C. Cottin-Bizonne, C. Ybert, E. Clément, *J. Phys.: Condens. Matter.* **2025**, *37*, 143501.
[42] D. P. Haeusser, W. Margolin, *Nat. Rev. Microbiol.* **2016**, *14*, 305.
[43] H. P. Erickson, D. E. Anderson, M. Osawa, *Microbiol. Mol. Biol. Rev.* **2010**, *74*, 504.
[44] S. Du, J. Lutkenhaus, *Trends Microbiol.* **2019**, *27*, 781.
[45] M. Osawa, D. E. Anderson, H. P. Erickson, *EMBO J.* **1998**, *17*, 462.
[46] K. D. Whitley, C. Jukes, N. Tregidgo, E. Karinou, P. Almada, Y. Cesbron, R. Henriques, C. Dekker, S. Holden, *Nat. Commun.* **2021**, *12*, 2448.
[47] H. P. Erickson, *Proc. Nat. Acad. Sci.* **2009**, *106*, 9238.
[48] P. Mateos-Gil, P. Tarazona, M. Vélez, *FEMS Microbiol. Rev.* **2019**, *43*, 73.
[49] X. Yang, Z. Lyu, A. Miguel, R. McQuillen, K. C. Huang, J. Xiao, *Science* **2017**, *355*, 744.
[50] J. Mingorance, G. Rivas, M. Vélez, P. Gómez-Puertas, M. Vicente, *Trends Microbiol.* **2010**, *18*, 348.
[51] G. Lan, A. Dajkovic, D. Wirtz, S. X. Sun, *Biophys. J.* **2008**, *95*, 4045.
[52] A. Páez, P. Tarazona, P. Mateos-Gil, M. Vélez, *Soft Matter* **2009**, *5*, 2625.
[53] D. A. García-Soriano, T. Heermann, A. Raso, G. Rivas, P. Schwille, *Sci. Rep.* **2020**, *10*, 10447.
[54] M. Osawa, D. E. Anderson, H. P. Erickson, *Science* **2008**, *320*, 792.
[55] I. López-Montero, P. López-Navajas, J. Mingorance, M. Vélez, M. Vicente, F. Monroy, *Biochim. Biophys. Acta* **2013**, *1828*, 687.
[56] I. López-Montero, P. Mateos-Gil, M. Sferrazza, P. López-Navajas, G. Rivas, M. Vélez, F. Monroy, *Langmuir* **2012**, *28*, 4744.
[57] D. A. Ramirez-Diaz, A. Merino-Salomón, F. Meyer, M. Heymann, G. Rivas, M. Bramkamp, P. Schwille, *Nat. Commun.* **2021**, *12*, 3310.
[58] E. Harry, L. Monahan, L. Thompson, *Int. Rev. Cytol.* **2006**, *253*, 27.
[59] Y. Li, J. Hsin, L. Zhao, Y. Cheng, W. Shang, K. C. Huang, H.-W. Wang, S. Ye, *Science* **2013**, *341*, 392.
[60] E. L. Meier, E. D. Goley, *Curr. Opin. Cell Biol.* **2014**, *26*, 19.
[61] P. G. de Gennes, *Scaling Cocepts in Polymer Physics*, Cornell University Press, NY USA, **1979**.
[62] P. Hotulainen, P. Lappalainen, *J. Cell Biol.* **2006**, *173*, 383.
[63] A. H. Brochu, S. Craig, *Biomaterials* **2010**, *96*, 492.
[64] W. M. Kier, K. K. Smith, *Zoological J. Linnean Soc.* **1985**, *83*, 307.
[65] Y. Forterre, J. M. Skotheim, J. Dumais, L. Mahadevan, *Nature* **2005**, *433*, 421.
[66] Q. Guo, E. Dai, X. Han, S. Xie, E. Chao, Z. Chen, *J. R. Soc. Interface* **2016**, *12*, 20150598.